



1 Predicting Deep-Seated Landslide Displacements in Mountains through the Integration of 2 Convolutional Neural Networks and Age of Exploration-Inspired Optimizer

3 Jui-Sheng Chou^{1,*}, Hoang-Minh Nguyen¹, Huy-Phuong Phan¹, Kuo-Lung Wang²

4 ¹ Department of Civil and Construction Engineering, National Taiwan University of Science and Technology, Taipei, Taiwan

5 ² Department of Civil Engineering, National Chi Nan University, Nantou, Taiwan

6 (jschou@mail.ntust.edu.tw; hoangminhkg1992@gmail.com; huyphuong777@gmail.com; klwang@ncnu.edu.tw)

7 *Correspondence e-mail address: jschou@mail.ntust.edu.tw

8 Abstract

9 Deep-seated landslides, becoming increasingly frequent due to changing climate patterns, pose significant
10 risks to human life and infrastructure. This research contributes to developing predictive early warning
11 systems for deep-seated slope displacements, employing advanced computational models for
12 environmental risk management. Our novel framework integrates machine learning, time series deep
13 learning, and convolutional neural networks (CNN), enhanced by the Age of Exploration-Inspired
14 Optimizer (AEIO) algorithm. Our approach demonstrates exceptional forecasting capabilities by utilizing
15 eight years of comprehensive data—including displacement, groundwater levels, and meteorological
16 information from the Lushan Mountain region in Taiwan. The AEIO-MobileNet model stands out for its
17 precision in predicting imminent slope displacements with a mean absolute percentage error (MAPE) of
18 2.81%. These advancements significantly enhance geohazard informatics by providing reliable and
19 efficient landslide risk assessment and management tools. These safeguard road networks, construction
20 projects, and infrastructure within vulnerable slope areas.

21 **Keywords:** deep-seated landslide; displacement forecasting; landslide risk assessment; early warning
22 system; machine learning; time-series deep learning; convolutional neural network; metaheuristic
23 optimization.

24 1. Introduction

25 The 378 landslides recorded worldwide between 1997 and 2017 resulted in the deaths of 18,414
26 people and left 4.8 million others injured, with associated costs estimated at around USD 8 billion
27 (Ageenko et al., 2022). Landslides represent a global hazard, particularly in developing countries, where
28 rapid urbanization, population growth, and significant land use changes occur (Caleca et al., 2024). The
29 identification, management, and monitoring of landslides are made difficult by the diversity of their types
30 (shallow slides, deep-seated slides, rock falls, rock slides, debris flows) and the complexity of their
31 categorization based on triggers, material composition, movement speed, and other characteristics (Das et



32 al., 2022; Hungr et al., 2014). These issues are further exacerbated in countries with complex geological
33 and climatic conditions.

34 Deep-seated landslides, or gravitational deformations, involve slow movement of soil or rock at
35 depths greater than 10m, impacting large areas and leading to significant debris flows (Dou et al., 2015).
36 Predicting these events is challenging and costly (Thai Pham et al., 2019). Therefore, extensive efforts
37 have been made to predict such disasters throughout history. One method that has been employed involves
38 thoroughly examining the physical and geological characteristics of the mountainous areas at risk of
39 landslides (Cotecchia et al., 2020). Furthermore, the level of groundwater has been shown by numerous
40 studies in the past to influence the mechanisms behind landslide formation significantly (Miao and Wang,
41 2023; Preisig, 2020). Consequently, in this study, groundwater levels will serve as inputs for models
42 designed to predict landslides.

43 In pursuing a generalized approach to landslide forecasting, researchers have determined that the
44 critical factors associated with slope instability exhibit temporal variability, necessitating using time series
45 data (Chae et al., 2017). This approach combines slope deformation data collected through sensors drilled
46 deep into the slope bed with data on the natural conditions of the monitoring area, which is collected
47 simultaneously. Upon establishing that the data pertinent to landslide prediction falls within the category
48 of time series data, a formidable challenge in research related to this type of disaster is devising a predictive
49 model capable of forecasting the likelihood of such catastrophes based on related factors.

50 One of the most effective solutions for constructing models to predict time series data involves
51 applying data-driven techniques. The advancement of computational capabilities has driven the
52 widespread adoption of data-driven machine-learning models over physics-based models. This shift is
53 based on the premise that the data used for slope monitoring originates from nonlinear systems (Zhou et
54 al., 2018). In contemporary times, an increasing array of novel data-driven solutions is being developed
55 to overcome the constraints of traditional machine-learning approaches. These CNN models, which excel
56 at automated feature extraction, can enhance efficiency in analyzing complex datasets and improve the
57 accuracy of prediction results (Alzubaidi et al., 2021).

58 Moreover, there is a noteworthy recent trend in employing metaheuristic optimization algorithms to
59 fine-tune the hyperparameters of artificial intelligence (AI) models, thereby augmenting their efficiency.
60 This approach has found application in geological and construction studies and other fields, showcasing
61 substantial effectiveness. Consequently, the fine-tuning of hyperparameters represents a potent avenue for
62 elevating the efficiency of AI models in research focused on predicting deep-seated displacements.

63 Leveraging the effective methodologies mentioned above, this study employs AI models optimized
64 by an innovative metaheuristic optimization algorithm to predict deep-seated landslides on the northern
65 slope of Lushan Mountain in Ren'ai Township, Nantou County. The geological characteristics of this area



66 have undergone extensive research. This research paper is firmly grounded in empirical evidence
67 meticulously collected over eight years from extensometers at depths of 70 and 40 meters. Our analysis
68 also considers the cumulative impact of storms and heavy rainfall on groundwater levels, utilizing data
69 from four stations measuring groundwater levels in the study area and other weather conditions that
70 potentially trigger landslides. The objectives of our research were as follows:

- 71 1) To analyze the application of machine learning and deep learning methods to time series data to forecast
72 short-term, deep-seated slope displacements across the Lushan Mountain area.
- 73 2) To identify the optimal model and hyperparameters for accurately forecasting deep-seated
74 displacements in the study area.
- 75 3) To evaluate the role of metaheuristic optimization algorithms in fine-tuning the hyperparameters of AI
76 models.

77 This study represents the first instance of AI models being utilized to predict deep-seated landslides
78 in Lushan Mountain. Additionally, it marks the inaugural application of AEIO for fine-tuning AI models
79 in landslide-related research. Our findings provide a valuable resource for civil engineers, contractors, and
80 inspectors involved in the planning and monitoring of construction projects in landslide-prone areas.
81 Predicting the likelihood of landslide events could assist in minimizing property loss, guiding schedule
82 adjustments, improving work safety, and ensuring smooth traffic flow during critical periods.

83 **2. Literature Review**

84 **2.1 Groundwater Levels and the Forecasting of Deep-Seated Displacements**

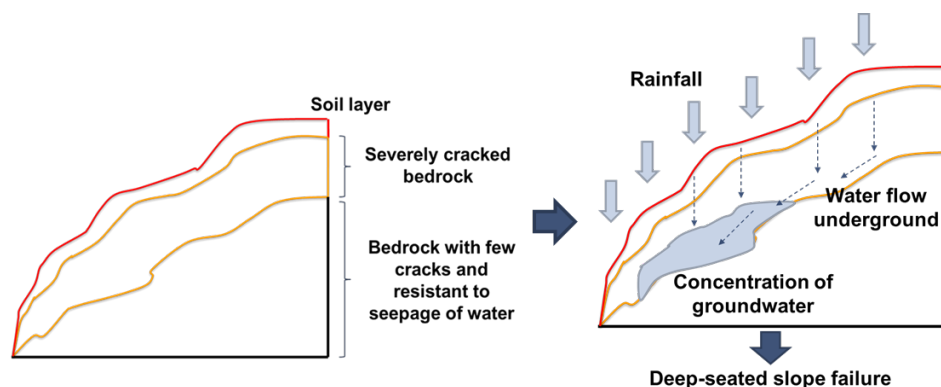
85 Landslide triggers can be attributed to loading, slope geometry, weather conditions, and
86 hydrological conditions (Perkins et al., 2024; Van Natijne et al., 2023; Millán-Arancibia and Lavado-
87 Casimiro, 2023; Jones et al., 2023). Among these, hydrological conditions, especially groundwater levels,
88 have been one of the most critical elements considered in studies related to landslide prediction (see Figure
89 1). Examples of this research include the Tessina landslide in northeastern Italy, where groundwater
90 conditions triggered movement (Petley et al., 2005). Additionally, the study by Keqiang et al. on water-
91 induced landslides in the Three Gorges Reservoir project area highlights the significant impact of
92 hydrological conditions on the likelihood of such disasters (Keqiang et al., 2015).

93 Similarly, Preisig developed a groundwater prediction model for analyzing the stability of a
94 compound slide in the Jura Mountains (Preisig, 2020). Additionally, Srivastava et al. explored machine
95 learning algorithms to forecast rainfall and established thresholds for landslide probabilities (Srivastava
96 et al., 2020). Although the research by Srivastava et al. did not directly rely on groundwater levels to
97 predict landslides, it is evident that rainfall, a crucial factor in their study for landslide prediction, also
98 influences hydrological conditions. Therefore, their research further underscores the importance of
99 considering groundwater levels in landslide prediction.



100 The northern slope in the Lushan area of central Taiwan, the region investigated in this study,
101 exhibits significant gravitational slope deformation, making it prone to landslides during typhoons or
102 heavy rainfall events. Lin et al. conducted in-depth studies on the mechanisms of landslide occurrence
103 based on the geological conditions of the area (Lin et al., 2020). While successfully providing valuable
104 insights into the evolution of deep-seated gravitational deformations, their research somewhat overlooked
105 the importance of hydrological conditions and groundwater levels in landslide formation.

106 To address the limitations of previous landslide research in the Lushan Mountain area, this study
107 will explore using hydrological conditions and groundwater levels as inputs for AI models to predict deep-
108 seated displacement, thus aiding in landslide forecasting in this region.



109
110 Figure 1. Schematic illustration showing the effects of groundwater on deep-seated slope failure

111 2.2 Forecasting Slope Displacements: Conventional Methods

112 Several conventional methods are commonly employed to predict deep slope displacement. These
113 methods primarily involve simulating factors affecting slope stability in landslide-prone areas using data
114 collected from ground-based monitoring devices. An early approach to predicting deep-seated slope
115 movements is geotechnical mapping. This technique characterizes rock and soil's strength, density, and
116 porosity.

117 For instance, Crosta et al. analyzed the geology and rock mass behavior using Voight's semi-
118 empirical failure criterion, incorporating time-dependent factors to generate velocity curves that indicate
119 risk levels (Crosta and Agliardi, 2003). Recently, Xu et al. (2018) utilized real-time remote monitoring
120 systems to measure internal stress, deep displacement, and surface strain. This data was used to formulate
121 forecasting models to assess slope stability, particularly in railway construction (Xu et al., 2018).

122 Moreover, physical-based numerical modeling methods, which simulate phenomena at a laboratory
123 scale, are also gaining traction in landslide research. These methods aim to maintain forecasts using
124 various data types while reducing human workload and ensuring high accuracy. For example, Mufundirwa
125 et al. conducted a laboratory study to examine the effectiveness of the inverse velocity model in predicting



126 rock mass destruction resulting from landslides at depths of 2m and 4m along the sliding plane. This study
127 utilized historically recorded data from Asamushi, Japan, and the Vaiont reservoir in Italy (Mufundirwa
128 et al., 2010). In another study, Wu et al. employed the numerical discontinuous deformation analysis
129 method to simulate a blocky assembly's post-failure behavior, incorporating earthquake seismic data (Wu,
130 2010). Meanwhile, Jiang et al. utilized fluid-solid coupling theory to simulate displacement, capturing the
131 interaction between fluid and solid materials (Jiang et al., 2011).

132 Stability analysis is another commonly used method related to physics, which evaluates the forces
133 acting on a slope behavior. W. Fu & Liao presented a technique for implementing the non-linear Hoek-
134 Brown shear strength reduction, determining the correlation between normal and shear stress based on the
135 Hoek-Brown criterion (Fu and Liao, 2010). Subsequently, the micro-units instantaneous friction angle and
136 cohesive strength under specific stress conditions are calculated. Although this approach effectively
137 addresses cost and labor issues, it still heavily relies on the researcher's assumptions and is limited by the
138 ability to utilize only a small portion of data from the research area.

139 However, in landslide studies, monitoring data is constantly updated, generating large volumes daily
140 with a temporal relationship (Peternel et al., 2022; Corominas et al., 2014). Hence, conventional methods
141 have shown limited success in handling big data, especially in identifying highly intricate samples that
142 require analysis of time series relationships or complex nonlinear associations.

143 **2.3 Forecasting Slope Displacements: Machine Learning and Deep Learning**

144 In studies employing machine learning and deep learning models for landslide research, a plethora
145 of research utilizes discrete data to train AI models to predict the probability of landslides or to construct
146 maps depicting landslide susceptibility. For instance, Margarint et al. employed a logistic regression
147 model to predict landslides based on discrete data in four regions of Romania (Margarint et al., 2013). The
148 logistic regression model yielded promising predictions, with an AUC value (area under the curve) ranging
149 between 0.851 and 0.94 for the validation dataset. Subsequently, these results were utilized to construct a
150 map of landslide susceptibility in the study area. In a similar study, Pham et al. utilized multiple AI models,
151 including support vector machines (SVM), logistic regression (LR), Fisher's linear discriminant analysis
152 (FLDA), Bayesian network (BN), and naïve Bayes (NB), for landslide susceptibility assessment in a
153 region within the Uttarakhand state of India (Pham et al., 2016). The SVM model yielded the best
154 prediction results among the models used.

155 In addition to discrete data, many landslide studies utilize time series data. When it comes to
156 technical forecasting using time series data, machine learning regression prediction models, such as
157 extreme learning machine (ELM) (Li et al., 2018), least squares support vector machine (LSSVM) (Liu
158 et al., 2019), dynamic neural network (DNN) (Aggarwal et al., 2020), random forests (RFs) (Hu et al.,
159 2021), SVM (Zhang et al., 2021), and Gaussian process regression (GPR) (Hu et al., 2019), have proven



160 highly effective at yielding reliable results. These models also provide scalability and the ability to handle
161 larger datasets. However, it is essential to note that machine learning models are sensitive to the white
162 noise typical of time series features. This can pose challenges in capturing subtle behaviors and complex
163 interrelationships, mainly when data availability is limited (Zhang et al., 2020). Finally, feature
164 engineering is computationally intensive and labor-intensive, limiting its applicability when rapid
165 forecasting is required.

166 Given that slope profiles and soil parameters are one-dimensional variables, a range of neural
167 network models, from simpler ones like Artificial Neural Networks (ANN) to more advanced approaches
168 such as Deep Neural Networks (DNNs) and CNN, can be employed to uncover the relationship between
169 slope stability and input parameters with minimal computational overhead (Fu et al., 2022). Additionally,
170 CNN models have been used in studies of this disaster. While CNN was initially designed for image
171 processing, its input and internal architecture are tailored for two-dimensional matrices, including the
172 convolution kernel and feature map. To address the one-dimensional nature of slope profiles and soil
173 physical and mechanical parameters, Pei, Meng, & Zhu developed a 1D-CNN model with dynamic inputs
174 to account for time-varying trigger factors (Pei et al., 2021). Their approach demonstrated superior
175 performance to conventional machine learning models regarding accuracy and robustness. However, it's
176 worth noting that this approach has yet to gain widespread adoption.

177 Moreover, another research trend in landslide forecasting involves the use of time series deep
178 learning models such as Recurrent Neural Networks (RNN), Long Short-Term Memory (LSTM), and
179 Gated Recurrent Units (GRUs), which use previous information to generate current outputs and provide
180 state feedback (Yang et al., 2019; Xu et al., 2022; Yang et al., 2022; Zhang et al., 2022). These time-series
181 deep learning models can effectively capture patterns of changes over time, making them highly suitable
182 for time-series data in landslide-related studies. However, there has yet to be a comprehensive study that
183 employs a combination of machine learning methods, time-series deep learning, and CNN models to
184 compare and determine the most suitable model for landslide prediction. Therefore, our research aims to
185 address this gap.

186 Another noteworthy research trend involves using AI models to predict landslides based on spatial-
187 temporal data. For instance, Dahal et al.'s study utilized spatial-temporal data to pinpoint where landslides
188 may occur and predict when they might happen and the expected landslide area density per mapping unit
189 (Dahal et al., 2024). The Ensemble Neural Network employed in this research yielded promising
190 predictions, demonstrating its potential for forecasting landslides in Nepal's areas affected by the Gorkha
191 Earthquake. However, our study only managed to gather temporal data. Consequently, the AI models
192 developed in our research will be trained to learn and forecast time-series data.

193 **2.4 Hybrid metaheuristic optimization algorithm and AI models in landslide prediction**



194 In landslide-related research, numerous studies have employed hybrid models, wherein metaheuristic
195 optimization algorithms optimize the hyperparameters of AI models. For example, Balogun et al. studied
196 landslide susceptibility mapping in Western Serbia (Balogun et al., 2021). This research collected 14
197 different condition factors to serve as input data for the Support Vector Regression (SVR) model to predict
198 landslide occurrences. The study results indicate that SVR models, with hyperparameters fine-tuned by
199 optimization algorithms such as gray wolf optimization (GWO), bat algorithm (BA), and cuckoo
200 optimization algorithm (COA), all yielded better prediction results compared to using a single model.

201 Hakim et al. conducted a study utilizing CNN models optimized by the GWO and imperialist
202 competitive algorithm (ICA) for landslide susceptibility mapping from geo-environmental and topo-
203 hydrological factors in Incheon, Korea (Hakim et al., 2022). This research demonstrates that GWO and
204 ICA effectively fine-tuned the CNN model, resulting in a highly accurate landslide susceptibility map.

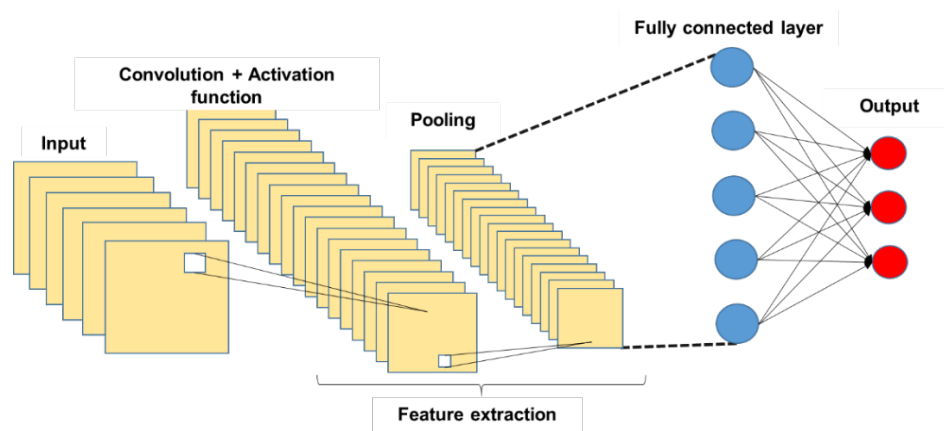
205 Jaafari et al. employed an AI model known as the group method of data handling (GMDH) for
206 classification purposes, optimizing it using the cuckoo search algorithm (CSA) and the whale optimization
207 algorithm (WOA). In northwest Iran, they aimed to predict landslides based on various factors, including
208 topographical, geomorphological, and other environmental factors (Jaafari et al., 2022). After training and
209 testing, the GMDH-CSA model produced superior prediction results compared to the GMDH-WOA and
210 the standalone GMDH model.

211 It is evident from numerous past studies on landslides that the application of metaheuristic
212 optimization algorithms significantly enhances the predictive effectiveness of AI models. Therefore, this
213 study also incorporates this approach to ensure the model's accuracy in landslide prediction. This study
214 will also employ a recently developed metaheuristic algorithm, including a clustering algorithm. This
215 algorithm is promising in yielding favorable results in fine-tuning hyperparameters for AI models.

216 **3. Methodology**

217 **3.1 Convolutional Neural Networks**

218 In 1998, LeCun introduced a novel type of DNN known as the CNN, specifically designed for
219 processing data with a grid-like structure, such as images. The complex, layered system of CNN facilitates
220 the automated extraction of features without extensive preprocessing, making it ideal for object
221 recognition, image classification, and segmentation tasks. The architecture of a typical CNN, as illustrated
222 in Figure 2, comprises an input layer (to receive image data), followed by hidden layers (including
223 convolutional, pooling, and fully connected layers), and concludes with the output layers. As depicted in
224 Figure 2, the complexity of CNN progressively increases from the convolutional layer to the fully
225 connected (FC) layer. This design enables CNN to recognize relatively simple patterns (lines, curves, etc.)
226 before progressing to capture more intricate features (faces, objects, etc.), with the ultimate aim of
227 extracting relevant information for accurate pattern identification.



228

229

Figure 2. Structure of basic CNN.

230

As illustrated in Figure 3, the convolutional layer is responsible for most computations in the network.

231

This involves extracting local features from an image using a set of learnable filters known as kernels.

232

The behavior of the filter in the convolutional layer is influenced by two main factors: stride and padding.

233

Stride refers to the pixel shift of the filter across the image, while padding aims to preserve information at

234

the corners. In each iteration, a portion of the image is convolved with a filter to generate a dot product of

235

pixels within its receptive field. This process is replicated across the entire image to produce a feature

236

map. The convolution operation is defined as follows:

237

$$C_i = b_i + \sum_{j=1}^{d_i} I_j * F_{ij}, \quad i = 1 \dots d_c \quad (1)$$

238

where C_i is the output of the convolutional layer or feature map, b_i is the bias, d_i is the depth of input, I_j

239

is the input image, F_{ij} is the filter, and d_c is the depth of the convolutional layer.

240

The multiplicative operations are usually followed by an activation function (the final element in the

241

convolutional layer), which introduces nonlinearity and creates intricate mappings between network

242

inputs and outputs. The activation function can be defined as follows:

243

$$Y_i = f(C_i) \quad (2)$$

244

where, Y_i is the output of the convolutional layer after the activation function, and f is the activation

245

function.

246

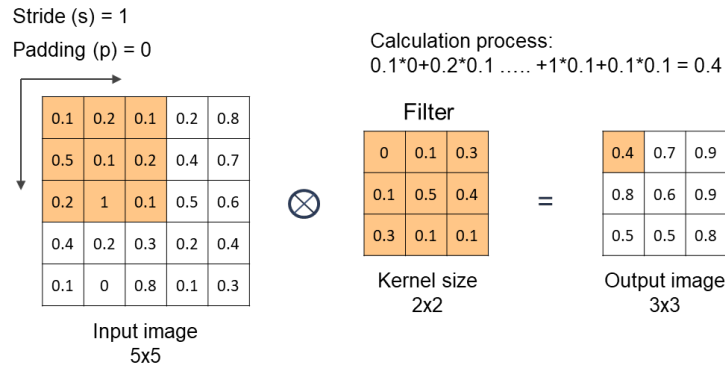
A rectified linear unit ReLU is a nonlinear CNN function with output $f(x) = \max(0, x)$. A ReLU

247

converts all negative values to zero or returns the original input values if the input exceeds zero. ReLU is

248

only one of many activation functions; however, it has proven to be the most effective overall.



249

250

Figure 3. Processing flow in convolution layer.

251

Pooling layers after the convolution layer can down-sample feature maps by summarizing features within the coverage area of a 2-D filter to reduce sensitivity to feature location, thereby improving resilience to changes in the position of features. Pooling layers also decrease the dimensions of the feature map, reducing the number of parameters to be dealt with, thereby decreasing computational overhead.

255

Output dimensions from the pooling layer are computed as follows:

256

$$\frac{c_w - f_w + 1}{s} * \frac{c_h - f_h + 1}{s} * c_n \quad (3)$$

257

where c_n is the number of channels in the feature map and $f_w * f_h$ indicate the width and height of the filter.

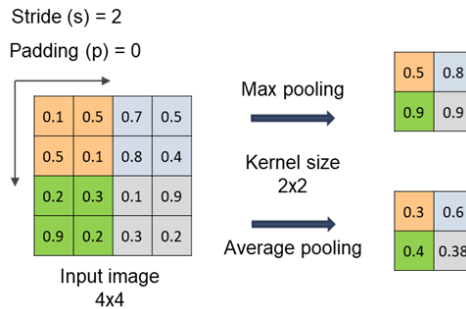
259

Max pooling and average pooling are commonly used in CNN. Max pooling accentuates salient features by selecting the maximum value within the filter's coverage area. In contrast, average pooling calculates the mean value within the exact location, providing a representative feature value. Illustrations of max pooling and average pooling are presented in Figure 4.

263

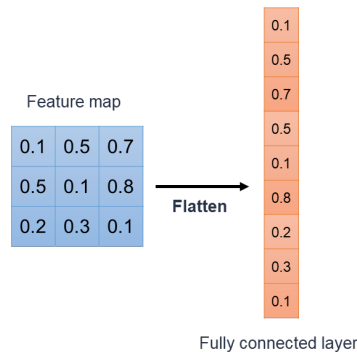
The final stage of a CNN comprises a series of fully connected (FC) layers. After the convolution and pooling operations, the feature map is flattened into a one-dimensional vector that connects to the FC layers, resembling an ANN. FC layers identify specific features, each represented by a neuron. In regression tasks, each neuron in the FC layer corresponds to a feature contributing to the final numerical output. The value transmitted by each neuron indicates its significance toward the regression result. FC layers are designed to predict the best continuous value for the target variable by combining and processing these neuron outputs. Figure 5 illustrates the structure of an FC layer.

269



270
 271

Figure 4. Max Pooling and Average Pooling.



272
 273

Figure 5. Structure of fully connected layer.

274 This study will use various CNN models to predict deep-seated slope displacement. The CNN models
 275 employed in this research include VGG (Simonyan and Zisserman, 2014), ResNet (He et al., 2016),
 276 Inception (Szegedy et al., 2016), Xception (Chollet, 2016), MobileNet (Kalenichenko et al., 2017),
 277 DenseNet (Huang et al., 2017), and NASNet (Zoph et al., 2018).

278 3.2 Deep Learning Models for Time Series

279 RNN was introduced by Elman in 1990 (Elman, 1990). This model makes predictions based on
 280 sequential data, crucial for language modeling, document classification, and time series analysis. The
 281 architecture of an RNN includes an input layer, a hidden layer with a variable number of RNN cells, and
 282 an output layer designed for label identification based on future displacement values. Figure 6 illustrates
 283 the structure of simple RNNs.

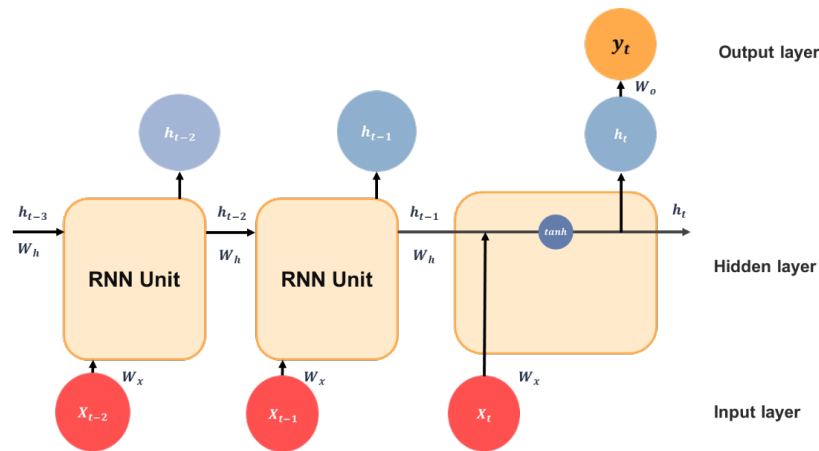
284 Each cell in an RNN acts as a memory cell, which is interconnected to enable the sequential transfer
 285 of time-dependent input information within a sliding window. This makes it possible to consider temporal
 286 correlations between events that may be widely separated in the time dimension. The following formula
 287 presents the hidden unit of standard RNNs at time t :

$$288 h_t = \tanh(W_x * x_t + W_h * h_{t-1} + b) \quad (4)$$

289 where x_t is the input vector at time t ; h_t is the output vectors of hidden units for
 290 time t ; W_x and W_h respectively indicate the input and interconnected weight matrices for the output of the



291 hidden layer; b is the bias term; and $\tanh()$ represents the hyperbolic tangent activation function, i.e.,
292 $\tanh(x) = \frac{1-e^{2x}}{1+e^{2x}}$. RNNs are well-suited to learning time series involving short-term dependencies.



293
294

Figure 6. Structure of basic RNNs.

295 In this study, advanced models of RNN, such as LSTM [54] and GRU [55], are also utilized, and
296 their effectiveness in predicting deep-seated landslides will be compared.

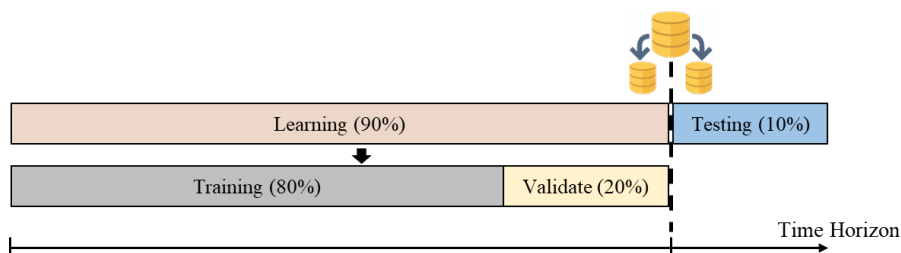
297 3.3 Machine Learning

298 In addition to the aforementioned deep learning models, as elucidated earlier, machine learning
299 models will be employed to predict deep-seated slope displacements in this research. The machine
300 learning models utilized will encompass the following: linear regression (LR) (Stanton, 2001), ANN
301 (McCulloch and Pitts, 2021), SVR (Drucker et al., 1996), classification and regression tree (CART)
302 (Breiman, 1984), radial basis function neural network (RBFNN) (Han et al., 2010), extreme gradient
303 boosting (XGBoost) (Chen; and Guestrin). These machine learning models will be used to make
304 predictions and will be compared with other deep learning models.

305 3.4 Model Validation and Performance Metrics

306 3.4.1 Evaluation and Validation

307 To obtain reliable (i.e., generalizable) evaluation and validation results, it is crucial that the data
308 used for testing does not include the data used for training. Therefore, a dataset must be divided into
309 training, validation, and testing subsets before training the AI model. Training data is used to learn patterns;
310 testing data is used to assess model performance and identify errors; and validation data is used to fine-
311 tune the hyperparameters. In the current study, we opted to refrain from employing cross-validation, which
312 tends to be time-consuming. Instead, we adopted the holdout approach to manage our large dataset with
313 well-represented target variables (Figure 7). A 90:10 ratio is generally used to split datasets into learning
314 and testing data (Di Nunno et al., 2023). When implementing the holdout method during hyperparameter
315 optimization, 20% of the learning data is used for validation, and the remaining 80% is used for training.



316

317

Figure 7. Data are splitting under the proposed Holdout scheme.

318

3.4.2 Performance Metrics

319

This study utilized four widely recognized performance measures to assess the model's effectiveness in prediction accuracy (Chou and Nguyen, 2023). The measures included mean absolute error (MAE), mean absolute percentage error (MAPE), and root mean square error (RMSE).

320

321

322

3.5 Age of Exploration-Inspired Optimizer

323

This study employs a range of AI models to forecast deep-seated displacement in mountainous regions. To enhance the prediction accuracy of these AI models, the study incorporates a novel metaheuristic optimization algorithm known as the Age of Exploration-Inspired Optimizer (AEIO). Developed by Chou and Nguyen in 2024, this algorithm has demonstrated high effectiveness in fine-tuning the hyperparameters of AI models. Figure 8 illustrates the AEIO algorithm.

324

325

326

327

328

The strength of the AEIO algorithm lies in its ability to develop specific strategies for particles based on their positions, enabling faster convergence to the optimal point. Using density-based spatial clustering of applications with noise (DBSCAN) for particle clustering, the AEIO determines whether particles are in favorable or unfavorable positions, reminiscent of explorers during the Age of Exploration. The proximity (within clusters) allows explorers to gather information and move toward optimal locations, thereby enhancing their ability to establish new colonies. In contrast, explorers far apart (outside clusters) adopt different strategies, relying on limited peer guidance or general trends in their quest for new territories.

329

330

331

332

333

334

335

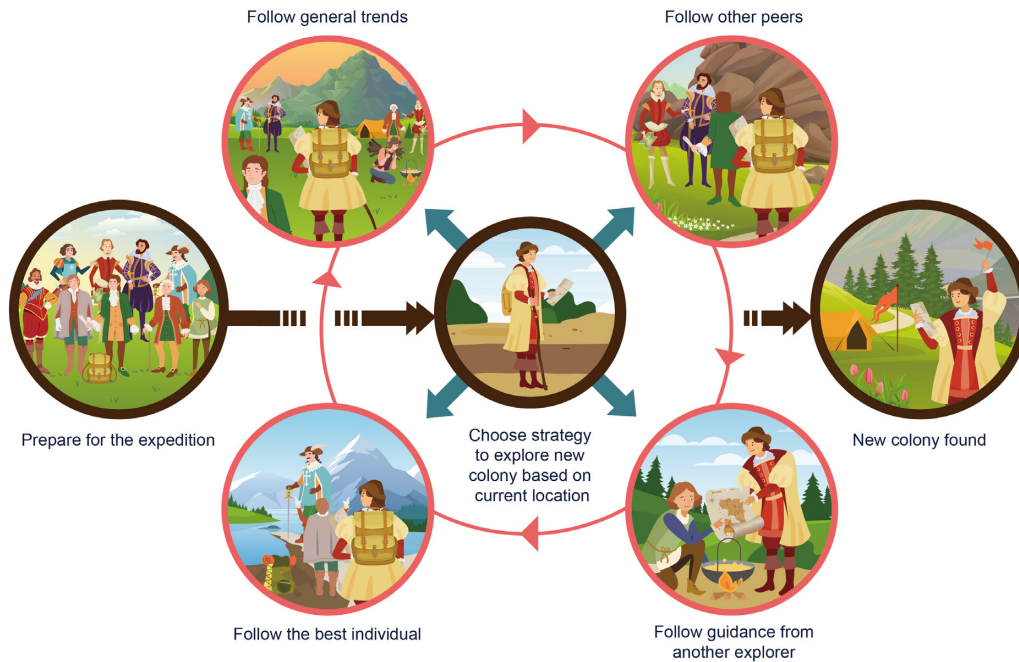


Figure 8. Illustration of Age of Exploration-Inspired Optimizer

336
 337

338 In each iteration, explorers forecast their next move. If it promises a better position, they relocate.
 339 Otherwise, if the new spot is less favorable for colony establishment, they stay put and await the next
 340 iteration. The algorithm employs specific mathematical formulas to calculate the movement step of
 341 explorers or particles in the AEIO.

342 • **Explorers follow general trends**

343 The explorer choosing this movement type will calculate the distance from their location to the
 344 center of all other explorers, then attempt to move towards that central point in the hope of finding a better
 345 location with the potential to establish a new colony. The following formula determines the explorer's
 346 position after the movement:

$$347 \quad x_{i,d}(t+1) = x_{i,d}(t) + \alpha * (Meanvl_d(t) - x_{i,d}(t)) \times rand(0,1) \times R \quad (5)$$

$$348 \quad Meanvl_d(t) = \frac{x_{1,d}(t) + x_{2,d}(t) + \dots + x_{n_{pop},d}(t)}{n_{pop}} \quad (6)$$

349 where $d = 1, 2, \dots, D$; D is the number of dimensions; $i = 1, 2, \dots, n_{pop}$; n_{pop} is the total number of
 350 explorers; $t = 1, 2, \dots, MaxIt$ is the number of iterations; $MaxIt$ is the maximum value of iteration; α is a
 351 parameter for adjusting the particle's movement toward the centroid position (usually equals 3).
 352 $Meanvl_d(t)$ is the centroid of all particles in dimension d . $rand(0,1)$ is the random number in the range
 353 $[0,1]$. R : a number that equals 1 or 2 depending on the value of $rand(0, 1)$ per the equation. $R =$
 354 $round(1 + rand(0,1) \times 1)$

355 • **Explorers follow three other peers**



356 Explorers employing this movement method will calculate the average position of three randomly
357 selected other explorers and then move toward this newly calculated average position. The explorer's new
358 position is computed using the following formula:

$$359 \quad x_{i,d}(t+1) = x_{i,d}(t) + \left(\frac{x_{1,d}(t) + x_{2,d}(t) + x_{3,d}(t)}{3} - x_{i,d}(t) \right) \times rand(0,1) \times R \quad (7)$$

360 where: $x_{1,d}(t)$, $x_{2,d}(t)$ and $x_{3,d}(t)$ are three random explorers in dimension d at iteration t .

361 ● **Explorers follow the best one**

362 According to this strategy, the explorer will move closer to the position of another explorer currently
363 holding the best position, as determined by the following formula:

$$364 \quad x_{i,d}(t+1) = x_{i,d}(t) + (Best_d(t) - x_{i,d}(t)) \times rand(0,1) \times R \quad (8)$$

365 where: $Best_d(t)$ represents the position of the particle with the best fitness in dimension d at iteration t .

366 ● **Explorers follow guidance from another one**

367 Explorers in favorable positions with access to information can execute this movement strategy. In
368 this scenario, explorers will consult with each other. The consulted explorer will compare their direction
369 and distance to the best individual, who holds the most favorable position and guide the inquirer. This
370 algorithm assumes that the inquirer can be any explorer, i.e., a random explorer. The following formula
371 describes how to calculate the new position of the explorer following this strategy:

$$372 \quad x_{i,d}(t+1) = x_{i,d}(t) + (Best_d(t) - x_{1,d}(t)) \times rand(0,1) \times R \quad (9)$$

373 ● **Crowd control mechanism**

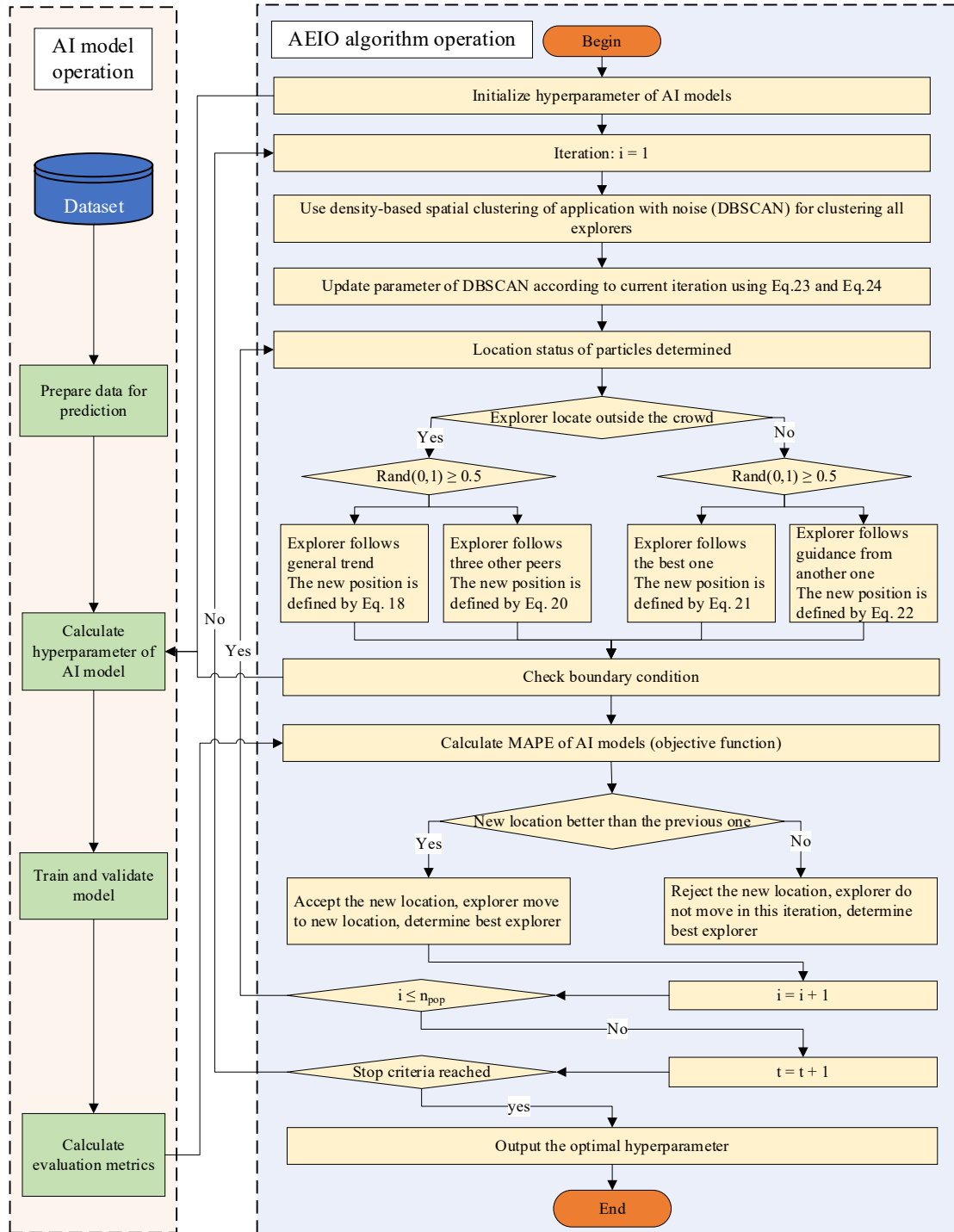
374 To enhance the efficiency of AEIO in transitioning between exploration and exploitation, a
375 mechanism is employed to adjust the parameters of DBSCAN throughout each cycle, according to the
376 following formula:

$$377 \quad \varepsilon_d = \left(0.1 + \frac{t}{MaxIt} \right) \times (Meanvl_d(t) - Best_d(t)) \quad (10)$$

$$378 \quad MinPts = round \left(1 + \frac{t}{MaxIt} \times 10 \right) \quad (11)$$

379 To fine-tune the hyperparameters of AI models, the AEIO algorithm treats each hyperparameter as
380 a variable. Furthermore, the objective function of the AEIO algorithm seeks to minimize the prediction
381 error of AI models, which is quantified by an evaluation metric (MAPE). Figure 9 presents a flowchart
382 illustrating the process by which the AEIO algorithm aids in fine-tuning hyperparameters for AI models.

383 **3.6 Experiment Setup**



384

385

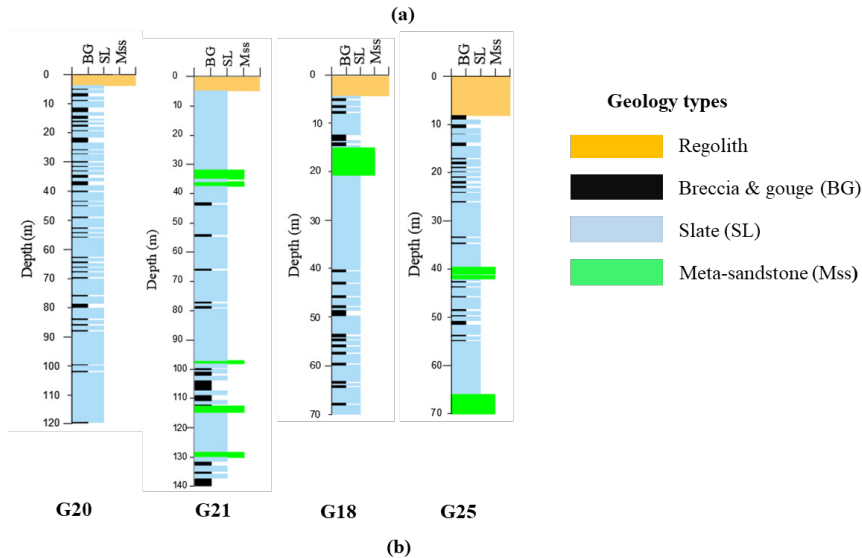
386

Figure 9. Flowchart of the fine-tuning process of AI models by the AEIO algorithm

3.6.1 Research Area



Image source: Imagery ©2022 CNES/Airbus, Maxar Technologies, Map data ©2022 Google



387

388

Figure 10. Illustration of (a) research location and (b) geological drilling survey

389

The current study focuses on the northern slope of Lushan hot spring in Ren'ai Township, Nantou County (Figure 10a), with Nenggao Mountain to the east, Hehuan Peaks to the north, Zhuoshe Mountain to the south, and Puli Basins to the west. The terrain features rugged mountain ranges, youthful valleys, and notable river erosion (Lee and Chi, 2011). Lushan Hot Springs is located below the hill, and the main access roads for nearby settlements and hot spring sites include Provincial Highway 14 and County Highway 87.

395

In an early study of deep landslides in this area, Lin et al. (Lin et al., 2020) reported that the Lushan slope exhibits large-scale deep-seated gravitational slope deformation, characterized by a steep scarp, a gently inclined head, and a curving river at its base. Figure 10b illustrates the geological details of the research area and shows the distribution of four survey boreholes (G20, G21, G18, and G25) along the slope. Regolith, slate, and meta-sandstone are three distinct lithological units revealed through drilling.

399



400 Initially, the thickness of the topmost regolith layer was found to be less than 10 meters. Secondly,
401 slate predominated, exhibiting a notable presence with sporadic evidence of weathering that resulted in
402 brecciated patterns. This composition frequently broke into breccia and gouges, particularly along
403 cleavage planes and thin shear zones, indicating its susceptibility to collapse. This geological layer is
404 identified as the area's primary cause of landslide risk. Finally, meta-sandstone appeared intermittent
405 compared to the more prevalent lithological units, characterized by its fragility and fractures and occurring
406 less frequently in the drilled samples.

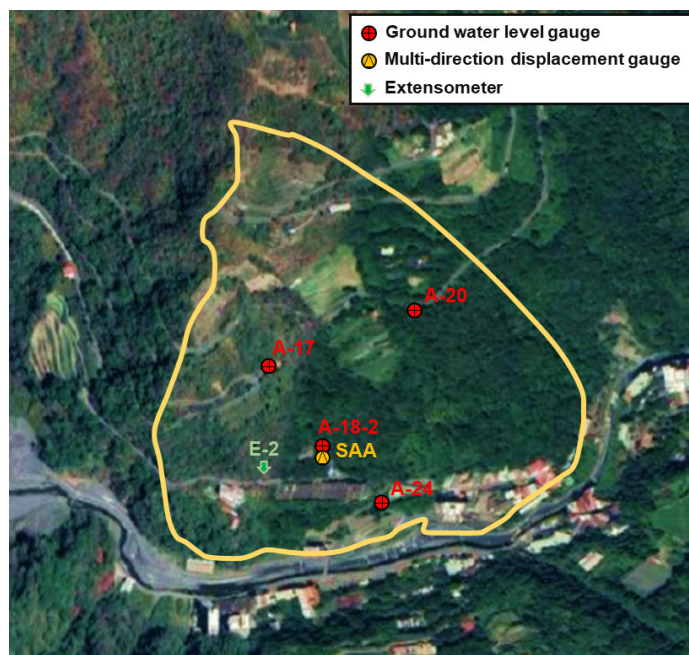
407 Previous research has detected signs of brittle deformation in the area. These indications include
408 chevron folds within cleavages, visible cracks, and intricate jigsaw puzzle-like patterns at the head of the
409 rock formations. Overturned and flexural toppling cleavages are prevalent towards the toe of the slope.
410 Additionally, kink bands are observable on cleavages that have recently undergone flexural folding along
411 the eastern boundary. Notably, horizontal cleavages near the toe region also exhibit inter-cleavage gouges.
412 These instances highlight the potential for significant geological changes and landslide risk in this region.

413 **3.6.2 Data Collection and Preprocessing**

414 In this study, hourly data of deep-seated displacement and groundwater level were collected by the
415 Department of Civil Engineering, College of Science and Technology, at the National Chi Nan University
416 research group over eight years from July 2009 to June 2017, yielding 68,317 data points. The installation
417 time points and locations are presented in Table 1 and Figure 11.

418 The data used in this study were collected using an in-hole telescopic gauge (E-2), a multidirectional
419 shape acceleration array sensor (SAA) with an underground displacement gauge, and four groundwater
420 level gauges (A-17, A-18-2, A-20, and A-24). The transmission, storage, and processing of data are
421 described in detail in the research of Lau et al. in 2023 (Lau et al., 2023).

422 The operation of the in-hole extensometer entailed the installation of a borehole through the sliding
423 surface. One end of a steel cable was anchored at the bottom, and a displacement gauge was placed at the
424 free end to measure deformations automatically. The fixed stops for E-2 and SAA were situated at depths
425 of 70 meters and 40 meters below the surface, respectively. In addition to groundwater level data,
426 information regarding significant rainfall events in this area was also measured and is presented in Table
427 2.



428

429

Image source: Imagery ©2022 CNES/Airbus, Maxar Technologies, Map data ©2022 Google

430

Figure 11. Locations of measurement devices

431

Table 1. Device installation timepoints

Year	2008	2009	2010	2011	2012	2013	2014	2015	2016	2017
Groundwater level gauge	A-17									
	No data						A-18-2			
	No data						A-20			
	No data						A-24			
Extensometer	No data						E-2			
	No data			SAA						

432

433

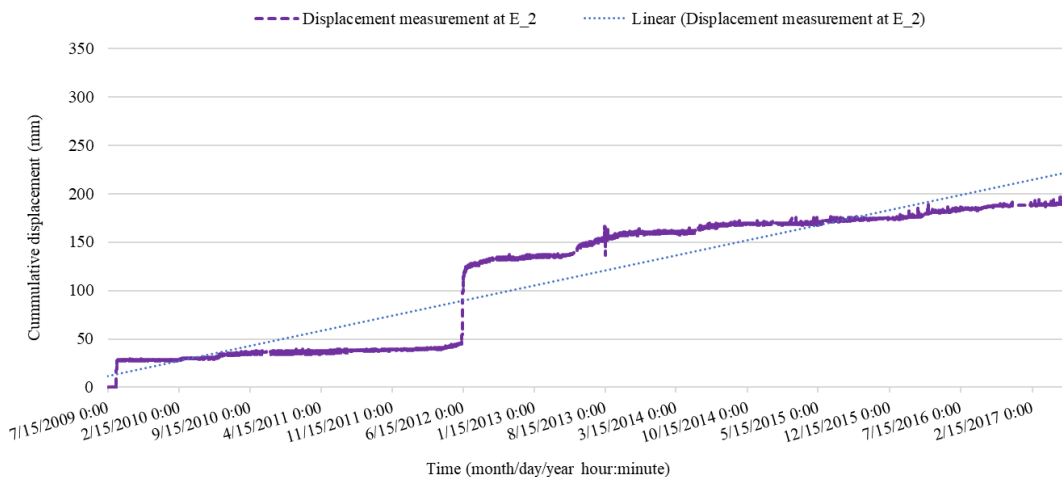
Table 2. Heavy rainfall events in the study area

No.	Rain onset (year/month/day/hour: minute)	Rain end time (year/month/day/hour: minute)	Accumulating rainfall (mm)	Drop rain hour (hr)	Event
1	7/17/2008 14:00	7/19/2008 21:00	418	55	Kameiji typhoon
2	9/11/2008 16:00	9/15/2008 12:00	943.5	92	Pungentmusc typhoon



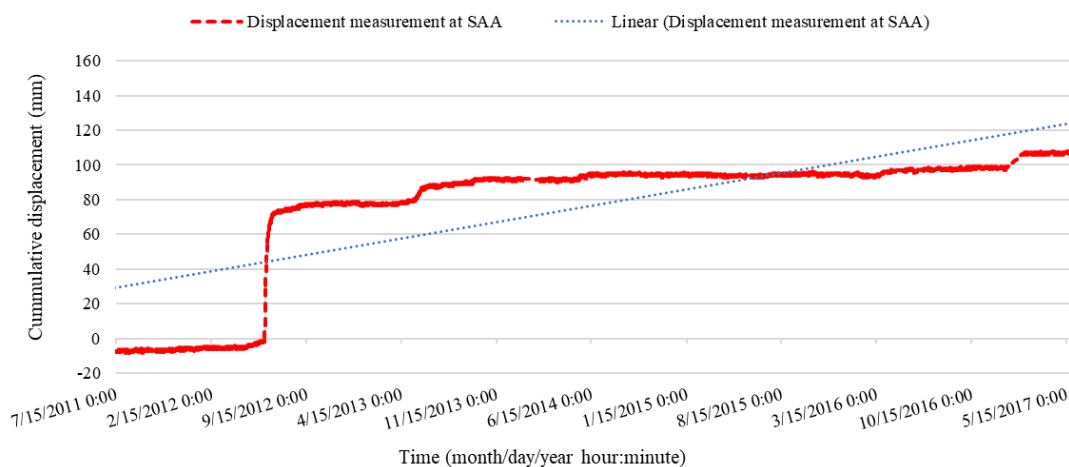
No.	Rain onset (year/month/day/hour: minute)	Rain end time (year/month/day/hour: minute)	Accumulating rainfall (mm)	Drop rain hour (hr)	Event
3	9/28/2008 1:00	9/30/2008 10:00	523.5	57	Rose honey typhoon
4	8/4/2009 3:00	8/12/2009 20:00	931	209	Mopull typhoon
5	6/8/2012 13:00	6/17/2012 16:00	1029	219	torrential rain
6	7/30/2012 7:00	8/3/2012 11:00	370	100	Supull typhoon
7	5/10/2013 16:00	5/25/2013 1:00	597	345	torrential rain
8	7/12/2013 19:00	7/15/2013 23:00	330	76	Suprofit typhoon
9	9/20/2013 22:00	9/23/2013 18:00	347	68	Usagi typhoon
10	5/9/2014 5:00	5/22/2014 3:00	326.5	310	torrential rain
11	7/22/2014 14:00	7/24/2014 0:00	321.5	34	Madham typhoon
12	6/1/2017 11:00	6/4/2017 21:00	897	82	torrential rain
13	6/11/2017 17:00	6/19/2017 3:00	638.5	178	torrential rain

434 Based on the collected data, analyses have examined the correlation between groundwater levels
 435 and deep-seated displacement at Lushan Mountain. To observe this correlation, graphs illustrating the
 436 variations in displacement (Figure 12 and Figure 13) and groundwater levels (Figure 14) over time have
 437 been plotted.



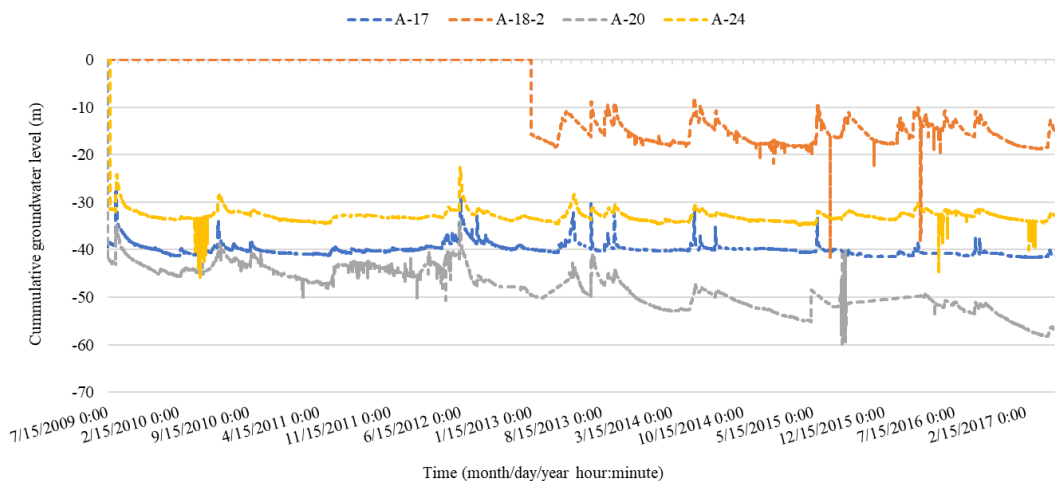
438
439

Figure 12. Time series data indicating measured displacements from extensometer E_2



440
441

Figure 13. Time series data indicating measured displacements from extensometer SAA



442

443

Figure 14. Groundwater levels at stations A-17, A-18-2, A-20, and A-24

444

The graphs above show that the displacement values at both stations often exhibit significant increases coinciding with periods of pronounced fluctuations in groundwater levels. Specifically, in June 2012, there was a notable surge in groundwater levels attributed to heavy rainfall from August 6, 2012, to August 17, 2012, totaling 1029 mm over 219 hours (as indicated in Table 2). The abnormal rise in groundwater levels caused a structural alteration in the area's soil, consequently amplifying deep-seated displacement at both stations, namely E_2 and SAA, as evidenced in Figure 12 and Figure 13.

450

Similar events occurred in November 2017. Heavy rainfall totaling 638.5 mm over 178 hours during this period also caused a sudden alteration in groundwater levels, resulting in significant deep-seated displacement. Through comparison, it is apparent that there were up to 13 instances of anomalous heavy rainfall during the study period. However, not every example of heavy rain resulted in significant fluctuations in groundwater levels, leading to substantial displacement. Hence, data regarding groundwater level elevation will be used to predict deep-seated landslides rather than rainfall data.

456

In addition to groundwater level data, weather factors such as temperature and humidity are also utilized as input data for the prediction model. These factors significantly impact the soil structure and can trigger substantial displacement or landslides. This study collected groundwater level and displacement data on-site using sensors. Furthermore, temperature and humidity data were obtained from the website <https://power.larc.nasa.gov>. This dataset is part of the Prediction of Worldwide Energy Resource (POWER) project, developed by the National Aeronautics and Space Administration (NASA) of the United States.

463

Table 3 displays the input and output variables for AI models to predict deep-seated displacement at Lushan Mountain. Two datasets will be generated: one for predicting displacement at the E_2 station and

464



465 another for indicating displacement at the SAA station. Table 4 outlines the number of data points for each
 466 dataset and illustrates how the data is divided into training and testing sets.

467 Table 3. Input and output variables of a model predicting deep-seated displacement.

	Attributes group	Attributes	Variable ID	Dataset of E_2 station	Dataset of SAA station
Output variables	Deep-seated displacement measures	Displacement extensometer at station E_2 (mm)	Y1	✓	-
		Displacement extensometer at station SAA (mm)	Y2	-	✓
Input variables	Groundwater level data	Groundwater level at station A-17 (m)	X1	✓	✓
		Groundwater level at station A-18-2 (m)	X2	✓	✓
		Groundwater level at station A-20 (m)	X3	✓	✓
		Groundwater level at station A-24 (m)	X4	✓	✓
	Weather data	Temperature at 2 meters (°C)	X5	✓	✓
		Specific humidity at 2 meters (g/kg)	X6	✓	✓

468 Table 4. Number of data points

Quantity of data points	Dataset of the E-2 station	Dataset of SAA station
Total data samples	68312	51679
Count of training samples (90% of the total sample)	61477 (2009/07/15-2016/09/07)	46523 (2011/07/13 – 2016/11/16)
Count of testing samples (10% of the total sample)	6835 (2016/09/07-2017/06/20)	5156 (2016/11/16-2017/06/20)

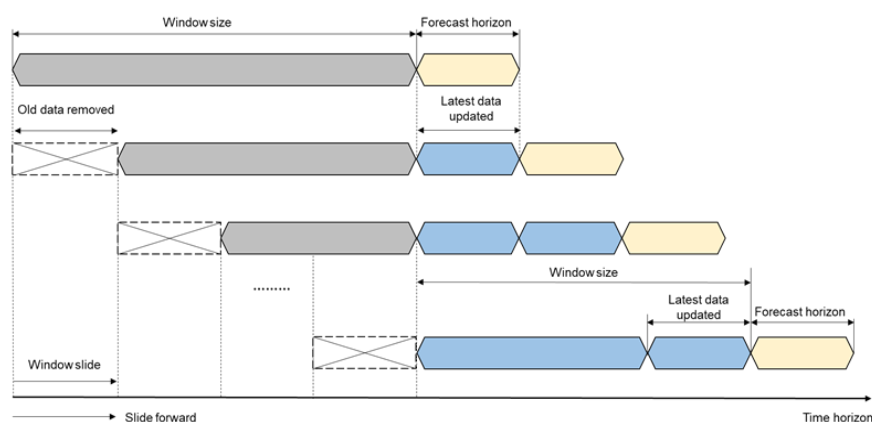
469 3.6.3 Data Preprocessing

470 Firstly, the data in this study will undergo a normalization process to scale all features to a consistent
 471 range (typically between 0 and 1). This step is essential to ensure that the model considers the importance
 472 of each feature, thereby enhancing overall prediction accuracy (Han et al., 2006).



473 In the current study, the sliding window technique is implemented after data normalization to
474 organize data according to a specific time frame. This involves using historical data from previous steps
475 to predict the output for subsequent steps (Chou and Ngo, 2016). The forecasting horizon refers to the
476 length of time into the future for which output forecasts are made.

477 The basic process of the sliding window technique is illustrated in Figure 15. To train AI models,
478 this study opts for a window size of one week (equivalent to 168 hours). This fixed window size is utilized
479 exclusively for single AI models. Subsequently, the hybrid model's AEIO algorithm and other
480 hyperparameters will fine-tune the window size to determine the most suitable settings.



481

482

Figure 15. Sliding window technique

483 This study focuses on predicting deep displacement values at two distinct time intervals: 1 day ahead
484 (+24 hours) and seven days ahead (+168 hours). These forecast horizons are strategically chosen to
485 provide timely information, enabling management departments to make accurate decisions regarding
486 evacuating people and assets from areas prone to landslides.

487 Specifically, for valuable assets and machinery that require time for relocation from landslide-prone
488 areas, having advance knowledge of the landslide event one week ahead of relocation is crucial.
489 Furthermore, for humans, animals, or other assets that can be evacuated more swiftly, predicting the
490 landslide one day in advance is sufficient to ensure safety.

491 The predicted outputs are quantified in mm/day, facilitating decision-making for administrators
492 according to the TGS-SLOPEM106 standard (Ruitang et al., 2017). Table 5 outlines suggested actions
493 corresponding to different degrees of deep displacement as per the TGS-SLOPEM106 standard issued by
494 the Taiwan government.

495 Table 5. Recommendations are taken from TGS-SLOPEM106 for addressing displacement values in the
496 early stages of deep sliding.



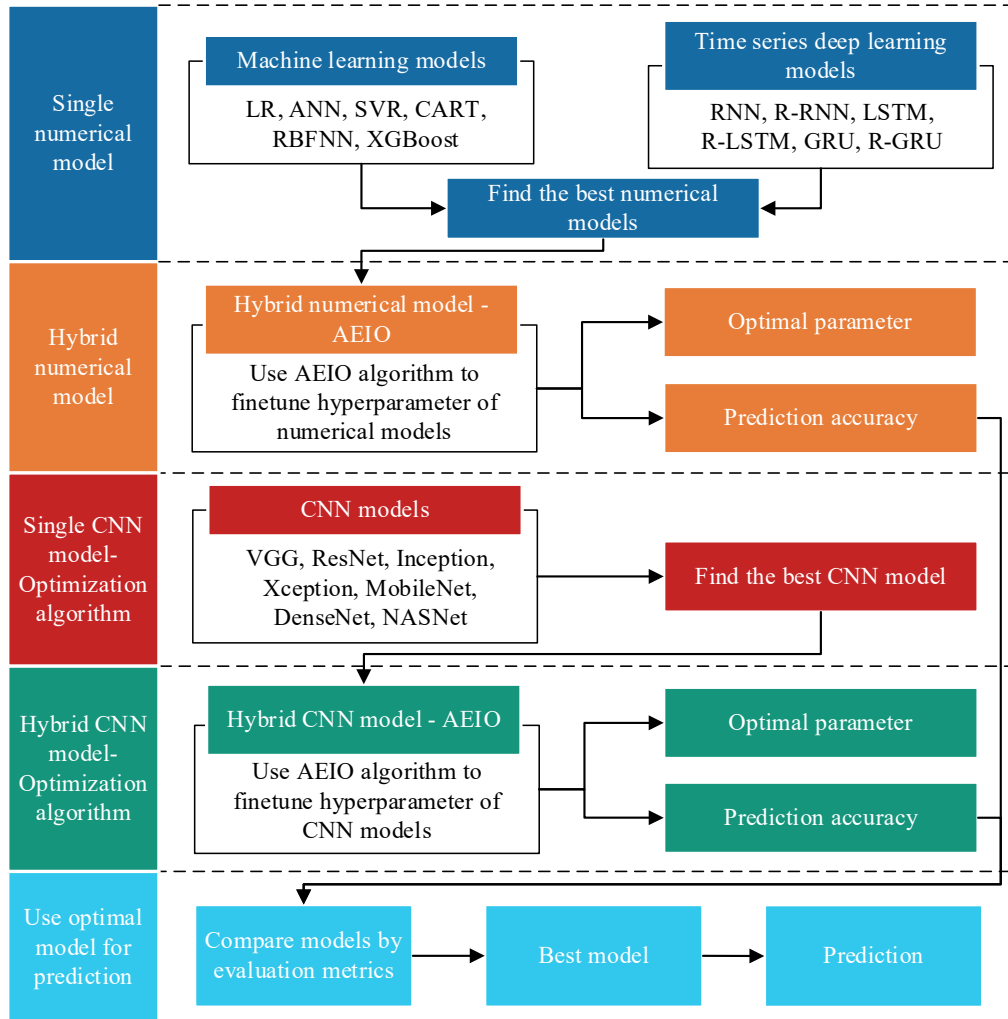
Classification of the displacement value	Attention value	Warning value	Action value
Corresponding displacement value	2 mm/month	0.5 mm/day	10 mm/day
Condition of slopes	The slope started to slip or slowly move	The hill is undergoing constant-velocity descent.	The rate of slope movement is increasing, elevating the risk of collapse.
Recommendations on monitoring activities	- Inspect the monitoring system for any irregularities and consider increasing the frequency of visual inspections	- Enhance the frequency of the automated monitoring system	- Implement a rigorous monitoring system frequency
Countermeasures	- Conduct a slope stability investigation and assessment - Develop a reinforcement and improvement plan to enhance slope stability	- Execute emergency slope reinforcement procedures - Develop an emergency response plan for individuals and vehicles within the landslide area	- Evacuate people and vehicles from the landslide area

497 **4. Model Establishment and Analysis Results**

498 **4.1 Model Establishment**

499 Predicting deep-seated landslides at Lushan Mountain is undoubtedly highly challenging, given that
 500 such landslides depend on numerous factors. Therefore, multiple methods will be employed
 501 simultaneously to identify the optimal AI model for prediction. These methods include single machine
 502 learning, time series deep learning, CNN, and hybrid models...

503 This study will conduct a testing process to systematically identify the optimal model capable of
 504 accurately predicting deep-seated landslides. An illustration of this process can be found in Figure 16.
 505 Initially, the study will sequentially employ various single numerical AI models, such as machine learning
 506 models (LR, ANN, SVR, CART, RBFNN, XGBoost) and time series deep learning models (RNN, R-
 507 RNN, LSTM, R-LSTM, GRU, R-GRU), to forecast displacement.



508

509

510

Figure 16. Diagram depicting the steps of choosing the optimal AI model to predict deep-seated landslide

511

Subsequently, the model with the highest prediction accuracy will be selected for integration with the AEIO algorithm, forming a hybrid model. In this hybrid model, the hyperparameters of the best numerical AI model will be fine-tuned by the AEIO algorithm to enhance prediction accuracy.

514

In addition to the numerical AI models, this study employs individual CNN models for predicting deep-seated displacement. Subsequently, similar to the approach above, the best CNN model with the highest displacement prediction capability will be fine-tuned by the AEIO algorithm within a hybrid model. In the final step, a comparison process between the two hybrid models— one comprising the best numerical model and the other involving the best CNN model fine-tuned by AEIO— will be conducted to select the optimal model for this study.

520

4.2 Analysis Results



521 This section will present the experimental results of the steps outlined in Figure 16, along with
 522 relevant metrics and analysis.

523 4.2.1 AI Models

524 a. Machine Learning Models

525 Initially, single machine learning models will be employed to predict deep-seated displacement. In
 526 this phase, machine learning models will utilize default hyperparameters, as detailed in Chou and
 527 Nguyen's research in 2023 (Chou and Nguyen, 2023). The prediction results of these models at both E-2
 528 and SAA stations are displayed in Table 6. These results show that most machine learning models
 529 demonstrate a relatively good predictive capability for displacement, particularly the XGBoost model,
 530 which exhibits MAPE values ranging from 8.14% to 9.58%. Following closely, CART also produces
 531 favorable prediction results, with MAPE ranging from 8.53% to 9.76%. Regarding prediction accuracy,
 532 XGBoost and CART models outperform LR, ANN, SVR, and RBFNN models.

533 Table 6. Performance results of machine learning models for predicting deep-seated displacement.

Model	MAPE (%)		MAE (mm)		RMSE (mm)		Time (s)	
	1-day-ahead	7-day-ahead	1-day-ahead	7-day-ahead	1-day-ahead	7-day-ahead	1-day-ahead	7-day-ahead
E-2-station								
LR	10.70	11.22	22.61	21.32	28.17	31.96	0.0001	0.003
ANN	12.31	13.31	22.19	24.92	26.56	32.54	129.80	212.83
SVR	12.46	12.47	21.98	22.56	26.27	28.05	162.55	174.44
CART	8.53	8.67	15.67	16.87	25.16	27.81	1.50	2.57
RBFNN	15.13	15.19	23.81	22.56	28.42	31.96	2.32	4.10
XGBoost	8.14	8.36	14.80	14.68	23.07	23.92	1.58	3.28
SAA-station								
LR	11.18	12.11	11.51	11.64	17.26	16.07	0.01	0.01
ANN	10.91	10.93	9.43	10.45	16.55	15.92	116.78	190.69
SVR	10.55	10.94	10.87	9.18	15.64	13.42	136.01	346.30
CART	10.57	10.76	7.11	7.30	13.51	10.63	0.91	1.59
RBFNN	14.51	14.95	11.38	12.68	17.13	19.06	4.20	8.76
XGBoost	9.17	9.58	8.43	7.83	16.36	16.97	1.12	2.29

534 Moreover, the results in Table 6 also indicate that there is not a significant difference in the prediction
 535 errors of the machine learning models at both E-2 and SAA stations, as the error values for both stations
 536 are nearly equal across all machine learning models. Regarding the running time, the LR model
 537 demonstrates the shortest duration, ranging from 0.001 to 0.1 seconds for all runs. However, the prediction



538 accuracy of this model could be higher, as mentioned earlier. In this case, the machine learning model
 539 with the longest running time is SVR, ranging from 136.01 to 346.3 seconds. This, combined with the low
 540 MAPE score, indicates that the SVR model operates inefficiently with the dataset in this study.

541 After reviewing the results of the machine learning models in this section, it is observed that
 542 XGBoost is the most suitable machine learning model for predicting deep-seated landslides, exhibiting
 543 both high prediction accuracy and a short running time. The following section will compare this model
 544 with the best time series deep learning model to select the optimal numerical model for fine-tuning.

545 **b. Time series deep learning models**

546 Similar to the machine learning models, in this section, the time series deep learning models will
 547 also be trained with default hyperparameters, as found in Chou and Nguyen's research in 2023 (Chou and
 548 Nguyen, 2023). The performance results of these models are shown in Table 7. Overall, akin to the
 549 machine learning models, the time series deep learning models also demonstrate fairly good prediction
 550 accuracy, especially the best model - R-GRU model, with MAPE ranging from 7.95 to 9.13%.

551 The performance of the R-GRU model surpasses that of the GRU model because the R-GRU model
 552 learns patterns from time series data in both forward and backward directions on the timeline, thereby
 553 capturing more patterns. Furthermore, the R-GRU model produces significantly better prediction results
 554 with a more complex learning mechanism than other time series deep learning models. However, due to
 555 its complex operational mechanism, the R-GRU model also requires more processing time than other time
 556 series deep learning models. From the results of Table 7, it is observed that the operating time of the R-
 557 GRU model ranges from 79.81 to 212.75 seconds.

558 From the conducted analyses, R-GRU has been identified as the best time series deep learning model,
 559 owing to its excellent prediction performance. Compared to the best machine learning model, XGBoost
 560 (with MAPE ranging from 8.14% to 9.58%), the R-GRU model (with MAPE ranging from 7.90 to 9.13%)
 561 demonstrates higher prediction accuracy. Therefore, the R-GRU model will be chosen as the best
 562 numerical AI model. R-GRU will undergo fine-tuning in the following section using the AEIO algorithm,
 563 further enhancing this model's accuracy.

564 Table 7. Performance results of time series deep learning models for predicting deep-seated displacement

Model	MAPE (%)		MAE (mm)		RMSE (mm)		Time (s)	
	1-day-ahead	7-day-ahead	1-day-ahead	7-day-ahead	1-day-ahead	7-day-ahead	1-day-ahead	7-day-ahead
E-2-station								
RNN	12.72	12.92	23.61	24.75	31.18	29.62	83.24	177.53
R-RNN	12.31	12.84	22.88	21.97	30.20	34.42	91.47	114.33
LSTM	8.42	8.57	17.87	16.31	21.41	22.98	123.10	151.91



Model	MAPE (%)		MAE (mm)		RMSE (mm)		Time (s)	
	1-day-ahead	7-day-ahead	1-day-ahead	7-day-ahead	1-day-ahead	7-day-ahead	1-day-ahead	7-day-ahead
R-LSTM	8.13	8.75	16.63	17.84	22.85	24.67	148.56	161.14
GRU	8.43	10.15	16.06	19.38	22.46	26.75	141.50	164.26
R-GRU	7.90	8.16	15.09	15.69	20.84	23.32	156.97	172.96
SAA-station								
RNN	11.92	13.98	17.61	12.65	25.71	23.19	36.77	60.31
R-RNN	14.60	14.73	18.77	13.85	26.19	24.97	49.26	59.06
LSTM	10.64	10.94	12.73	12.25	29.21	29.57	62.84	113.76
R-LSTM	10.14	10.35	11.77	11.60	26.10	27.48	70.94	87.48
GRU	9.32	9.28	18.05	18.11	25.26	22.41	69.56	211.77
R-GRU	8.03	9.13	18.84	17.85	21.57	21.86	79.81	212.75

565

566 4.2.2 Best AI Model Finetuned by AEIO Algorithm

567 This section will focus on fine-tuning the hyperparameters of the numerical model to enhance its
 568 performance in predicting deep-seated landslides. The AEIO algorithm will fine-tune the hyperparameters
 569 of the study's best numerical AI model, the R-GRU model. Details regarding the names and search ranges
 570 of the hyperparameters are outlined in Table 8. The objective function of the AEIO algorithm during the
 571 fine-tuning process is to minimize the MAPE value of the R-GRU model.

572 Table 9 illustrates the results of the fine-tuning process. From this table, it is observed that the AEIO
 573 algorithm has successfully identified the optimal hyperparameters of the R-GRU model, significantly
 574 improving the prediction accuracy of this model. For instance, the MAPE in predicting 1-day-ahead
 575 displacement of R-GRU before fine-tuning was 7.9%, but this number decreased to only 3.03% after fine-
 576 tuning. All other predictions similarly show a decreasing trend.

577 Fine-tuning the R-GRU model using AEIO will maximize its potential, minimizing the prediction
 578 error to the lowest possible level. Therefore, the results obtained in this section reflect the actual quality
 579 of the dataset as well as the level of difficulty in prediction. Specifically, based on the results in Table 9,
 580 it is observed that the predictions for one-day ahead displacement (with MAPE of 3.03% and 3.94%)
 581 consistently outperform those for seven-days ahead displacement (with MAPE of 6.38% and 7.96%).

582 One-day-ahead predictions have a shorter time horizon, making them less affected by environmental
 583 fluctuations and making changes more accessible to predict. Conversely, in the case of seven-day-ahead
 584 displacement prediction, this timeframe is long enough for various factors, such as weather conditions and
 585 human interventions, to occur, increasing uncertainty and volatility in the predicted figures.



586 Additionally, Table 9 indicates that predictions from the dataset of the E-2 station consistently
 587 outperform those of the SAA station. Specifically, the displacement prediction at the E-2 station is 3.03%
 588 and 6.38%, better than the corresponding numbers for the SAA station, which are 3.94% and 7.96%,
 589 respectively. This is attributed to the dataset collected by the E-2 station being more comprehensive and
 590 gathered over a more extended period than the SAA station (as shown in Table 4).

591 Table 10 presents the optimal hyperparameters identified by the AEIO algorithm. Furthermore, in
 592 terms of running time, most models, after fine-tuning, exhibit longer running times compared to the
 593 original model. However, this increase is entirely acceptable since the additional running time is minimal,
 594 and the benefits of fine-tuning are significant, as mentioned above, aiding in the model's more efficient
 595 operation.

596 Table 8. Search ranges of the hyperparameters of the optimal hybrid numerical models (Chou and Nguyen,
 597 2023).

Hybrid model	Hyperparameter	Search range
AEIO-R-GRU	Window size	[1-720]
	Number of hidden units	[1-400]
	Learning rate	[0.0001, 0.5]
	Dropout	[0.00, 0.99]
	Number of epochs	[10, 120]
	Batch size	[32, 64]

598 Table 9. Performance results of hybrid time-series deep learning model with AEIO in deep-seated
 599 landslide prediction

	Model	MAPE (%)	MAE (mm)	RMSE (mm)	Time (s)
One-day- ahead displacement prediction	E-2-station				
	AEIO-R-GRU	3.03	6.89	17.98	196
	SAA-station				
	AEIO-R-GRU	3.94	4.16	11.20	184
Seven-day- ahead of displacement prediction	E-2-station				
	AEIO-R-GRU	6.38	10.02	18.05	261
	SAA-station				
	AEIO-R-GRU	7.96	12.49	7.82	248

600

601 Table 10. Optimal hyperparameter of time series deep learning model found by AEIO algorithm



	Model	Window size	Number of hidden units	Dropout rate	Learning rate	Number of epochs	Batch size
One-day-ahead displacement prediction	E-2-station						
	AEIO-R-	41	81	0.27	0.7	18	64
	GRU						
	SAA- station						
	AEIO-R-	54	145	0.19	0.46	32	32
	GRU						
Seven-day-ahead of displacement prediction	E-2- station						
	AEIO-R-	97	164	0.24	0.61	20	32
	GRU						
	SAA- station						
	AEIO-R-	69	147	0.28	0.31	17	32
	GRU						

602 4.2.3 CNN Models

603 This section presents the results of utilizing CNN models, including VGG, ResNet, Inception,
 604 Xception, DenseNet, and NASNet, to predict deep-seated landslide displacement. The CNN models in
 605 this part use the default settings (Chou and Nguyen, 2023). Table 11 displays the prediction error results
 606 of the CNN models for one-day-ahead and seven-day-ahead forecasts for both E-2 and SAA stations.

607 The prediction results demonstrate that most CNN models produce highly accurate predictions.
 608 Specifically, predictions made by VGG, ResNet, MobileNet, DenseNet, and Inception exhibit MAPE
 609 values below 5%. Among these, MobileNet and DenseNet201 emerge as the two models with the highest
 610 accuracy. For one-day-ahead prediction, the best model for predicting displacement at the E-2 station is
 611 MobileNet, with a MAPE of 4.11%, and the best model for predicting displacement at the SAA station is
 612 DenseNet201, with a MAPE of 6.36%. For seven-day-ahead prediction, the best model for predicting
 613 displacement at the E-2 station is DenseNet201, with a MAPE of 5.3%, and the best model for predicting
 614 displacement at the SAA station is MobileNet, with a MAPE of 6.8%. These models will be selected
 615 accordingly for fine-tuning in the subsequent section.

616 Regarding running time, the CNN models in this section exhibit significantly longer running times
 617 compared to the numerical models in the previous sections. For example, the running time of the best
 618 CNN model to predict one-day-ahead displacement at the E-2 station—MobileNet—is 1.21 hours. In
 619 contrast, the running time of the best single numerical model for predicting this index is 159.97 seconds.



620 While CNN models yield better prediction results, considering their extended running times, users
 621 need to weigh practical considerations before opting for this type of model. For instance, CNN models
 622 should be employed in cases requiring accurate predictions for research and measurement purposes.
 623 Conversely, numerical models like R-GRU are more suitable for real-time predictions and computations
 624 on low-performance devices.

625 Table 11. Performance results of the CNN models for deep-seated displacement prediction

Model	MAPE (%)		MAE (mm)		RMSE (mm)		Time (hour)	
	1-day-ahead	7-day-ahead	1-day-ahead	7-day-ahead	1-day-ahead	7-day-ahead	1-day-ahead	7-day-ahead
E-2- station								
VGG16	4.58	7.38	12.73	13.97	26.54	35.69	3.03	3.31
VGG19	4.47	6.30	12.53	15.11	25.74	32.82	3.14	2.82
ResNet50V2	4.87	7.68	15.28	12.52	31.82	27.19	2.99	3.44
ResNet101V2	4.61	6.60	9.81	9.08	34.67	32.74	2.24	2.96
ResNet152V2	4.71	6.46	7.26	12.60	21.13	19.08	2.94	2.05
InceptionV3	4.99	7.30	11.18	11.65	32.97	34.92	2.43	3.27
InceptionRestNetV2	13.32	15.78	22.51	27.08	76.75	61.11	3.22	3.08
Xception	5.27	7.34	11.60	10.20	35.86	30.68	2.94	3.29
MobileNet	4.11	8.92	12.22	13.62	47.43	31.72	1.21	1.44
DenseNet121	11.15	11.13	16.30	21.49	37.68	46.51	3.32	3.99
DenseNet169	4.74	7.86	11.44	12.20	17.09	36.28	3.02	3.52
DenseNet201	4.66	5.30	8.11	7.44	21.82	10.39	2.09	2.29
NASNetMobile	13.82	15.91	31.00	19.52	46.07	55.65	2.53	3.13
NASNetLarge	13.20	34.23	20.46	61.81	61.52	75.39	3.89	3.93
SAA- station								
VGG16	5.76	7.90	6.07	12.76	9.48	8.95	3.14	3.36
VGG19	5.95	7.32	9.14	13.45	11.68	7.03	3.55	3.20
ResNet50V2	9.87	9.35	12.43	13.81	15.71	9.75	4.57	3.83
ResNet101V2	8.48	17.68	10.56	19.36	11.47	21.94	3.54	3.40
ResNet152V2	9.43	11.42	12.32	10.35	14.91	13.27	3.35	3.88
InceptionV3	10.96	8.11	12.73	9.13	14.48	12.71	3.80	3.18
InceptionRestNetV2	9.86	11.08	13.51	16.75	18.04	21.59	3.23	2.91



Model	MAPE (%)		MAE (mm)		RMSE (mm)		Time (hour)	
	1-day-ahead	7-day-ahead	1-day-ahead	7-day-ahead	1-day-ahead	7-day-ahead	1-day-ahead	7-day-ahead
Xception	7.42	7.28	7.82	7.08	10.13	10.47	3.48	3.60
MobileNet	7.12	6.80	8.28	9.92	11.58	13.83	1.43	2.13
DenseNet121	8.69	11.69	8.56	14.39	12.54	15.76	3.93	3.42
DenseNet169	6.55	9.56	6.16	9.61	11.08	15.51	3.60	3.76
DenseNet201	6.36	10.45	7.46	11.62	9.37	14.51	2.51	3.13
NASNetMobile	10.31	22.12	13.86	62.04	18.95	43.51	3.56	2.88
NASNetLarge	10.25	13.69	11.20	14.05	15.95	19.09	3.18	3.34

626 4.2.4 Best CNN Models Finetuned by AEIO Algorithm

627 In this section, as analyzed in part 4.2.3, the AEIO algorithm will sequentially fine-tune CNN models
 628 to enhance prediction accuracy. Table 12 illustrates the search range of hyperparameters for the CNN
 629 models to be fine-tuned. Table 13 presents the performance results of the CNN models after being fine-
 630 tuned.

631 However, a challenge in this section is that CNN models primarily analyze and learn from image
 632 data. Therefore, numerical data must be converted into image data before training. This poses a challenge
 633 because current computer hardware may need to be fully capable of efficiently converting numerical data
 634 into images for each computation. Hence, this study utilizes the optimal window sizes previously
 635 identified for fine-tuning numerical models (Table 10) for this scenario and employs these fixed window
 636 sizes for CNN models.

637 The results of the fine-tuning process demonstrate that the AEIO has successfully identified the
 638 optimal hyperparameters for the CNN models, enhancing their accuracy. For instance, in the case of the
 639 MobileNet model used for one-day-ahead prediction at the E-2 station, the fine-tuning process reduced
 640 the MAPE of this model from 4.11% to 2.81%. A similar trend is also observed in the remaining prediction
 641 scenarios.

642 Furthermore, similar to the case of AEIO-R-GRU, the CNN models exhibit the same trend, where
 643 one-day-ahead predictions are more accurate than seven-day-ahead predictions. Similarly, forecasts at the
 644 E-2 station demonstrate higher accuracy than predictions at the SAA station. The rationale for this has
 645 been explained in section 4.2.2. Lastly, the optimal hyperparameters of each CNN model, identified by
 646 the AEIO algorithm, are presented in Table 14. Compared to models in previous sections, CNN models
 647 with optimal hyperparameters obtained in this section exhibit the most minor errors, indicating that these
 648 are the most effective models in this study for predicting landslide occurrences.



649 Table 12. Search ranges of the hyperparameters of the optimal hybrid numerical models (Chou and
 650 Nguyen, 2023).

Hybrid model	Hyperparameter	Search range
AEIO-CNN	Learning rate	[0.00, 0.1]
	Decay	[0.00, 0.1]
	Momentum	[0.00, 0.99]
	Epsilon	[1.0e-7, 0.001]
	Dropout	[0.00, 0.99]
	Epochs	[10, 120]
	Batch size	[32, 64]

651 Table 13. Performance results of best CNN models with AEIO in deep-seated landslide prediction

	Model	MAPE (%)	MAE (mm)	RMSE (mm)	Time (hour)
One-day-ahead displacement prediction	E-2-station				
	AEIO-MobileNet	2.81	5.09	11.92	1.25
	SAA-station				
Seven-day-ahead of displacement prediction	AEIO-DenseNet201	3.30	6.32	15.65	3.48
	E-2-station				
	AEIO-DenseNet201	4.30	5.32	15.65	3.48
Seven-day-ahead of displacement prediction	SAA-station				
	AEIO-MobileNet	5.63	9.35	14.27	3.39

652

653 Table 14. Optimal hyperparameter of CNN models found by AEIO algorithm

	Model	Learning rate	Decay	Momentum	Epsilon	Dropout	Epochs	Batch size
One-day-ahead displacement prediction	E-2-station							
	AEIO-MobileNet	0.0011	0.00095	0.00001	3.0e-7	0.56	15	64
	SAA-station							
One-day-ahead displacement prediction	AEIO-DenseNet201	0.00012	0.0012	0.00011	1.0e-7	0.49	16	64
	E-2-station							



	Model	Learning rate	Decay	Momentum	Epsilon	Dropout	Epochs	Batch size
Seven-day-ahead of displacement prediction	AEIO-	0.0012	0.0011	0.00022	1.0e-7	0.51	15	64
	DenseNet201							
	SAA-station							
	AEIO-	0.00014	0.00098	0.00011	2.0e-7	0.50	14	64
	MobileNet							

654 4.3 Discussion

655 This study centers on landslides in Lushan Mountain, Taiwan, adopting a fundamentally different
 656 approach than previous research. While past studies primarily focused on constructing AI models for
 657 classification, calculating the probability of landslide occurrences, and generating landslide susceptibility
 658 maps (Balogun et al., 2021; Hakim et al., 2022; Jaafari et al., 2022), our study is oriented towards
 659 predicting displacement to provide warnings about potential landslide hazards.

660 As utilized in our calculations, computing deep-seated displacement offers several benefits. Firstly,
 661 understanding internal displacements provides accurate information for engineers to assess the resilience
 662 of structures and infrastructure in at-risk areas, facilitating the issuance of sensible warnings. Secondly,
 663 forecasting deep-seated displacement offers insights into the severity of the disaster, aiding in effective
 664 evacuation and rescue planning.

665 Moreover, unlike AI models in previous studies (Balogun et al., 2021; Hakim et al., 2022; Jaafari et
 666 al., 2022), our research incorporates machine learning, time series deep learning, and CNN models,
 667 utilizing metaheuristic optimization algorithms to fine-tune their hyperparameters. However, the novelty
 668 of our study lies in adopting pre-trained models, such as MobileNet, DenseNet, Inception, and VGG,
 669 rather than conventional CNN models. The practicality of employing these pre-trained models has
 670 demonstrated effectiveness in predicting displacement in this research.

671 The models developed in this study demonstrate predictive solid capabilities for deep-seated
 672 displacement. Among them, the AEIO-MobileNet model is the most effective, achieving predictions with
 673 deficient error, indicated by a MAPE of 2.81%. However, these models' practical applicability in real-
 674 world scenarios must be improved due to the time-consuming processes involved in data collection,
 675 processing, and AI model operation, making timely predictions challenging. Meanwhile, there have been
 676 studies that successfully built real-time landslide detection systems (Wang et al., 2023; Das et al., 2020;
 677 C. et al., 2021). We acknowledge this limitation of our study. Therefore, future research endeavors will
 678 aim to address this issue.

679 5. Conclusion and Recommendations



680 This study addresses the persistent threat of landslides, a primary concern due to their severe impact
681 on lives and property. Employing various AI models, such as machine learning, time series deep learning,
682 CNN models, and metaheuristic optimization algorithms, the research focuses on predicting deep-seated
683 landslides at Lushan Mountain in Ren'ai Township, Nantou County. The study aims to enhance early
684 prediction accuracy by utilizing eight years of displacement and groundwater level data from Lushan
685 Mountain and weather data from the POWER project. The predictions cover one-day and seven-day
686 intervals, serving diverse purposes in landslide forecasting for timely evacuation. The research explores
687 single and hybrid AI models to determine the most effective approach. The following conclusions are
688 drawn from this research:

689 (a). CNN models optimized by the novel AEIO algorithm yield the best prediction results. In particular,
690 AEIO-MobileNet predicts one-day-ahead displacement at the E-2 station with a MAPE score of only
691 2.81%, demonstrating high accuracy.

692 (b). While CNN models boast high prediction accuracy, their computational time is also considerable.
693 Therefore, decisions regarding their usage should also consider real-world constraints.

694 (c). The AEIO-R-GRU model also yields reasonably good prediction results, although not on par with
695 CNN models. The best result achieved by the AEIO-R-GRU model is a MAPE of 3.03% for one-day-
696 ahead prediction at the E-2 station.

697 (d). The AEIO algorithm has successfully fine-tuned hyperparameters for AI models. Especially in the
698 case of predicting one-day-ahead displacement, it has aided the MobileNet model in improving its
699 predictive capability by 31.6%, enabling this model to provide more accurate predictions.

700 (e). The prediction results from the E-2 station consistently outperform those from the SAA station. This
701 is attributed to the fact that data from the E-2 station has been collected over a longer and more
702 comprehensive period.

703 (f). The study results demonstrate that AI models can accurately predict deep-seated displacement, which
704 can be implemented in real-world scenarios.

705 **Declare of Competing Interest**

706 The authors declare that there are no known conflicts of interest associated with this publication, and
707 there has been no significant financial support for this work that could have influenced its outcome.

708 **Data Availability Statement**

709 The data and source codes supporting this study's findings are available at
710 <https://www.researchgate.net/profile/Jui-Sheng-Chou> and from the corresponding author upon reasonable
711 request.

712 **Acknowledgments**



713 The authors thank the National Science and Technology Council (NSTC), Taiwan, for financially
714 supporting this research under NSTC grants 112-2221-E-011-033-MY3 and 111-2221-E-011-037-MY3.

715 **Author contribution**

716 Jui-Sheng Chou: conceptualization, methodology, supervision, writing manuscript, reviewing, and
717 editing. Hoang-Minh Nguyen: data processing, coding, and writing manuscript. Huy-Phuong Phan: Data
718 processing, coding, and manuscript writing. Kuo-Lung Wang: data preparation, supervision, and
719 reviewing.

720 **References**

721 Ageenko, A., Hansen, L. C., Lyng, K. L., Bodum, L., and Arsanjani, J. J.: Landslide Susceptibility
722 Mapping Using Machine Learning: A Danish Case Study, *Isprs Int J Geo-Inf*, 11,
723 <https://doi.org/10.3390/ijgi11060324>, 2022.

724 Aggarwal, A., Alshehri, M., Kumar, M., Alfarraj, O., Sharma, P., and Pardasani, K. R.: Landslide data
725 analysis using various time-series forecasting models, *Comput Electr Eng*, 88,
726 <https://doi.org/10.1016/j.compeleceng.2020.106858>, 2020.

727 Alzubaidi, L., Zhang, J., Humaidi, A. J., Al-Dujaili, A., Duan, Y., Al-Shamma, O., Santamaría, J., Fadhel,
728 M. A., Al-Amidie, M., and Farhan, L.: Review of deep learning: concepts, CNN architectures, challenges,
729 applications, future directions, *Journal of Big Data*, 8, 53, <https://doi.org/10.1186/s40537-021-00444-8>,
730 2021.

731 Balogun, A. L., Rezaie, F., Pham, Q. B., Gigovic, L., Drobnjak, S., Aina, Y. A., Panahi, M., Yekeen, S.
732 T., and Lee, S.: Spatial prediction of landslide susceptibility in western Serbia using hybrid support vector
733 regression (SVR) with GWO, BAT and COA algorithms, *Geosci Front*, 12,
734 <https://doi.org/10.1016/j.gsf.2020.10.009>, 2021.

735 Breiman, L.: *Classification and Regression Trees*, Taylor & Francis Group, New York,
736 <https://doi.org/10.1201/9781315139470>, 1984.

737 C., P., R., A., Kanwar, V. S., and B., N.: Design and Development of Real-time landslide early warning
738 system through low cost soil and rainfall sensors, *Materials Today: Proceedings*, 45, 5649-5654,
739 <https://doi.org/10.1016/j.matpr.2021.02.456>, 2021.

740 Caleca, F., Scaini, C., Frodella, W., and Tofani, V.: Regional-scale landslide risk assessment in Central
741 Asia, *Nat Hazard Earth Sys*, 24, 13-27, <https://doi.org/10.5194/nhess-24-13-2024>, 2024.

742 Chae, B.-G., Park, H. J., Catani, F., Simoni, A., and Berti, M.: Landslide prediction, monitoring and early
743 warning: a concise review of state-of-the-art, *Geosciences Journal*, 21, 1033-1070,
744 <https://doi.org/10.1007/s12303-017-0034-4>, 2017.

745 Chen, T. and Guestrin, C.: XGBoost: A Scalable Tree Boosting System, In *Proceedings of the 22nd ACM
746 SIGKDD International Conference on Knowledge Discovery and Data Mining*, New York, NY, USA,
747 785–794, <https://doi.org/10.1145/2939672.2939785>, 2016.

748 Chollet, F.: Xception: Deep Learning with Depthwise Separable Convolutions, 2017 IEEE Conference on
749 Computer Vision and Pattern Recognition (CVPR), Honolulu, HI, USA, July 21 2017,
750 <https://doi.org/10.48550/arXiv.1610.02357>, 2017.

751 Chou, J. S. and Ngo, N. T.: Time series analytics using sliding window metaheuristic optimization-based
752 machine learning system for identifying building energy consumption patterns, *Appl Energy*, 177, 751-770,
753 <https://doi.org/10.1016/j.apenergy.2016.05.074>, 2016.



- 754 Chou, J. S. and Nguyen, N. Q.: Forecasting Regional Energy Consumption via Jellyfish Search-Optimized
755 Convolutional-Based Deep Learning, *Int J Energ Res*, Volume 2023,
756 <https://doi.org/10.1155/2023/3056688>, 2023.
- 757 Corominas, J., van Westen, C., Frattini, P., Cascini, L., Malet, J. P., Fotopoulou, S., Catani, F., Van Den
758 Eeckhaut, M., Mavrouli, O., Agliardi, F., Pitolakis, K., Winter, M. G., Pastor, M., Ferlisi, S., Tofani, V.,
759 Hervás, J., and Smith, J. T.: Recommendations for the quantitative analysis of landslide risk, *Bulletin of*
760 *Engineering Geology and the Environment*, 73, 209-263, <https://doi.org/10.1007/s10064-013-0538-8>,
761 2014.
- 762 Cotecchia, F., Santaloia, F., and Tagarelli, V.: Towards A Geo-Hydro-Mechanical Characterization of
763 Landslide Classes: Preliminary Results, *Applied Sciences*, 10, <https://doi.org/10.3390/app10227960>, 2020.
- 764 Crosta, G. B. and Agliardi, F.: Failure forecast for large rock slides by surface displacement measurements,
765 *Canadian Geotechnical Journal*, 40, 176-191, <https://doi.org/10.1139/t02-085>, 2003.
- 766 Dahal, A., Tanyas, H., Westen, C. v., Meijde, M. v. d., Mai, P. M., Huser, R., and Lombardo, L.: Space-
767 time landslide hazard modeling via Ensemble Neural Networks, *Nat Hazard Earth Sys*, 24, 823-845,
768 <https://doi.org/10.5194/nhess-24-823-2024>, 2024.
- 769 Das, K., Majumdar, S., Moulik, S., and Fujita, M.: Real-Time Threshold-based Landslide Prediction
770 System for Hilly Region using Wireless Sensor Networks, 2020 IEEE International Conference on
771 Consumer Electronics - Taiwan (ICCE-Taiwan), Taoyuan, Taiwan, [https://doi.org/10.1109/ICCE-](https://doi.org/10.1109/ICCE-Taiwan49838.2020.9258181)
772 [Taiwan49838.2020.9258181](https://doi.org/10.1109/ICCE-Taiwan49838.2020.9258181), 2020.
- 773 Das, S., Sarkar, S., and Kanungo, D. P.: Rainfall-induced landslide (RFIL) disaster in Dima Hasao, Assam,
774 Northeast India, *Landslides*, 19, 2801-2808, <https://doi.org/10.1007/s10346-022-01962-z>, 2022.
- 775 Di Nunno, F., de Marinis, G., and Granata, F.: Short-term forecasts of streamflow in the UK based on a
776 novel hybrid artificial intelligence algorithm, *Scientific Reports*, 13, 7036,
777 <https://doi.org/10.1038/s41598-023-34316-3>, 2023.
- 778 Dou, J., Paudel, U., Oguchi, T., Uchiyama, S., and Hayakawa, Y. S.: Shallow and Deep-Seated Landslide
779 Differentiation Using Support Vector Machines: A Case Study of the Chuetsu Area, Japan, *Terr Atmos*
780 *Ocean Sci*, 26, 227-239, [https://doi.org/10.3319/Tao.2014.12.02.07\(Eosi\)](https://doi.org/10.3319/Tao.2014.12.02.07(Eosi)), 2015.
- 781 Drucker, H., Burges, C. J. C., Kaufman, L., Smola, A., and Vapnik, V.: Support vector regression
782 machines, *NIPS'96: Proceedings of the 9th International Conference on Neural Information Processing*
783 *Systems*, 155-161, 1996.
- 784 Elman, J. L.: Finding Structure in Time, *Cognitive Sci*, 14, 179-211, [https://doi.org/10.1016/0364-](https://doi.org/10.1016/0364-0213(90)90002-E)
785 [0213\(90\)90002-E](https://doi.org/10.1016/0364-0213(90)90002-E), 1990.
- 786 Fu, W. X. and Liao, Y.: Non-linear shear strength reduction technique in slope stability calculation,
787 *Comput Geotech*, 37, 288-298, <https://doi.org/10.1016/j.compgeo.2009.11.002>, 2010.
- 788 Fu, Y., Lin, M., Zhang, Y., Chen, G., and Liu, Y.: Slope stability analysis based on big data and
789 convolutional neural network, *Frontiers of Structural and Civil Engineering*, 16, 882-895,
790 <https://doi.org/10.1007/s11709-022-0859-4>, 2022.
- 791 Hakim, W. L., Rezaie, F., Nur, A. S., Panahi, M., Khosravi, K., Lee, C. W., and Lee, S.: Convolutional
792 neural network (CNN) with metaheuristic optimization algorithms for landslide susceptibility mapping in
793 Icheon, South Korea, *J Environ Manage*, 305, <https://doi.org/10.1016/j.jenvman.2021.114367>, 2022.
- 794 Han, H. G., Chen, Q. L., and Qiao, J. F.: Research on an online self-organizing radial basis function neural
795 network, *Neural Comput Appl*, 19, 667-676, <https://doi.org/10.1007/s00521-009-0323-6>, 2010.



- 796 Han, J., Kamber, M., and Pei, J.: Data Mining: Concepts and Techniques, Southeast Asia Edition, Morgan
797 Kaufmann Publishers Inc., San Francisco, CA, United States, 696 pp., [https://doi.org/10.1016/C2009-0-](https://doi.org/10.1016/C2009-0-61819-5)
798 [61819-5](https://doi.org/10.1016/C2009-0-61819-5), 2006.
- 799 He, K., Zhang, X., Ren, S., and Sun, J.: Deep Residual Learning for Image Recognition, 2016 IEEE
800 Conference on Computer Vision and Pattern Recognition, <https://doi.org/10.48550/arXiv.1512.03385>,
801 2016.
- 802 Hu, B., Su, G., Jiang, J., Sheng, J., and Li, J.: Uncertain Prediction for Slope Displacement Time-Series
803 Using Gaussian Process Machine Learning, Ieee Access, PP, 1-1,
804 <https://doi.org/10.1109/ACCESS.2019.2894807>, 2019.
- 805 Hu, X. L., Wu, S. S., Zhang, G. C., Zheng, W. B., Liu, C., He, C. C., Liu, Z. X., Guo, X. Y., and Zhang,
806 H.: Landslide displacement prediction using kinematics-based random forests method: A case study in
807 Jinping Reservoir Area, China, Eng Geol, 283, <https://doi.org/10.1016/j.enggeo.2020.105975>, 2021.
- 808 Huang, G., Liu, Z., Maaten, L. v. d., and Weinberger, K. Q.: Densely Connected Convolutional Networks,
809 2017 IEEE Conference on Computer Vision and Pattern Recognition (CVPR),
810 <https://doi.org/10.1109/CVPR.2017.243>, 2017.
- 811 Hungr, O., Leroueil, S., and Picarelli, L.: The Varnes classification of landslide types, an update,
812 Landslides, 11, 167-194, <https://doi.org/10.1007/s10346-013-0436-y>, 2014.
- 813 Jaafari, A., Jaafari, A., Panahi, M., Panahi, M., Mafi-Gholami, D., Mafi-Gholami, D., Rahmati, O.,
814 Rahmati, O., Shahabi, H., Shahabi, H., Shirzadi, A., Shirzadi, A., Lee, S., Lee, S., Bui, D. T., Bui, D. T.,
815 Pradhan, B., and Pradhan, B.: Swarm intelligence optimization of the group method of data handling using
816 the cuckoo search and whale optimization algorithms to model and predict landslides, Appl Soft Comput,
817 116, <https://doi.org/10.1016/j.asoc.2021.108254>, 2022.
- 818 Jiang, J., Ehret, D., Xiang, W., Rohn, J., Huang, L., Yan, S., and Bi, R.: Numerical simulation of Qiaotou
819 Landslide deformation caused by drawdown of the Three Gorges Reservoir, China, Environmental Earth
820 Sciences, 62, 411-419, <https://doi.org/10.1007/s12665-010-0536-0>, 2011.
- 821 Jones, J. N., Bennett, G. L., Abanco, C., Matera, M. A. M., and Tan, F. J.: Multi-event assessment of
822 typhoon-triggered landslide susceptibility in the Philippines, Nat Hazard Earth Sys, 23, 1095-1115,
823 <https://doi.org/10.5194/nhess-23-1095-2023>, 2023.
- 824 Kalenichenko, A. G. H. M. Z. B. C. D., Wang, W., Weyand, T., Andreetto, M., and Adam, H.: MobileNets:
825 Efficient Convolutional Neural Networks for Mobile Vision Applications, CoRR, abs/1704.04861,
826 <https://doi.org/10.48550/arXiv.1704.04861>, 2017.
- 827 Keqiang, H., Zhiliang, W., Xiaoyun, M., and Zengtao, L.: Research on the displacement response ratio of
828 groundwater dynamic augment and its application in evaluation of the slope stability, Environmental Earth
829 Sciences, 74, 5773-5791, <https://doi.org/10.1007/s12665-015-4595-0>, 2015.
- 830 Lau, Y. M., Wang, K. L., Wang, Y. H., Yiu, W. H., Ooi, G. H., Tan, P. S., Wu, J., Leung, M. L., Lui, H.
831 L., and Chen, C. W.: Monitoring of rainfall-induced landslides at Songmao and Lushan, Taiwan, using
832 IoT and big data-based monitoring system, Landslides, 20, 271-296, [https://doi.org/10.1007/s10346-022-](https://doi.org/10.1007/s10346-022-01964-x)
833 [01964-x](https://doi.org/10.1007/s10346-022-01964-x), 2023.
- 834 Lee, Y. F. and Chi, Y. Y.: Rainfall-induced landslide risk at Lushan, Taiwan, Eng Geol, 123, 113-121,
835 <https://doi.org/10.1016/j.enggeo.2011.03.006>, 2011.
- 836 Li, H., Xu, Q., He, Y., and Deng, J.: Prediction of landslide displacement with an ensemble-based extreme
837 learning machine and copula models, Landslides, 15, 2047-2059, [https://doi.org/10.1007/s10346-018-](https://doi.org/10.1007/s10346-018-1020-2)
838 [1020-2](https://doi.org/10.1007/s10346-018-1020-2), 2018.



- 839 Lin, H. H., Lin, M. L., Lu, J. H., Chi, C. C., and Fei, L. Y.: Deep-seated gravitational slope deformation
840 in Lushan, Taiwan: Transformation from cleavage-controlled to weakened rockmass-controlled
841 deformation, *Eng Geol*, 264, <https://doi.org/10.1016/j.enggeo.2019.105387>, 2020.
- 842 Liu, C. Y., Jiang, Z. S., Han, X. S., and Zhou, W. X.: Slope displacement prediction using sequential
843 intelligent computing algorithms, *Measurement*, 134, 634-648,
844 <https://doi.org/10.1016/j.measurement.2018.10.094>, 2019.
- 845 Margarint, M. C., Grozavu, A., and Patriche, C. V.: Assessing the spatial variability of coefficients of
846 landslide predictors in different regions of Romania using logistic regression, *Nat Hazard Earth Sys*, 13,
847 3339-3355, <https://doi.org/10.5194/nhess-13-3339-2013>, 2013.
- 848 McCulloch, W. and Pitts, A.: A Logical Calculus of the Ideas Immanent in Nervous Activity (1943), *Ideas
849 That Created the Future*, 79-88, <https://doi.org/10.1007/BF02478259>, 2021.
- 850 Miao, H. B. and Wang, G. H.: Prediction of landslide velocity and displacement from groundwater level
851 changes considering the shear rate-dependent friction of sliding zone soil, *Eng Geol*, 327,
852 <https://doi.org/10.1016/j.enggeo.2023.107361>, 2023.
- 853 Millán-Arancibia, C. and Lavado-Casimiro, W.: Rainfall thresholds estimation for shallow landslides in
854 Peru from gridded daily data, *Nat Hazard Earth Sys*, 23, 1191-1206, <https://doi.org/10.5194/nhess-23-1191-2023>, 2023.
- 856 Mufundirwa, A., Fujii, Y., and Kodama, J.: A new practical method for prediction of geomechanical
857 failure-time, *Int J Rock Mech Min*, 47, 1079-1090, <https://doi.org/10.1016/j.ijrmms.2010.07.001>, 2010.
- 858 Pei, H., Meng, F., and Zhu, H.: Landslide displacement prediction based on a novel hybrid model and
859 convolutional neural network considering time-varying factors, *Bulletin of Engineering Geology and the
860 Environment*, 80, 7403-7422, <https://doi.org/10.1007/s10064-021-02424-x>, 2021.
- 861 Perkins, J. P., Oakley, N. S., Collins, B. D., Corbett, S. C., and Burgess, W. P.: Characterizing the scale
862 of regional landslide triggering from storm hydrometeorology, *Nat Hazard Earth Sys*,
863 <https://doi.org/10.5194/egusphere-2024-873>, 2024.
- 864 Peternel, T., Janža, M., Šegina, E., Bezak, N., and Maček, M.: Recognition of Landslide Triggering
865 Mechanisms and Dynamics Using GNSS, UAV Photogrammetry and In Situ Monitoring Data, *Remote
866 Sensing*, 14, <https://doi.org/10.3390/rs14143277>, 2022.
- 867 Petley, D. N., Mantovani, F., Bulmer, M. H., and Zannoni, A.: The use of surface monitoring data for the
868 interpretation of landslide movement patterns, *Geomorphology*, 66, 133-147,
869 <https://doi.org/10.1016/j.geomorph.2004.09.011>, 2005.
- 870 Pham, B. T., Pradhan, B., Bui, D. T., Prakash, I., and Dholakia, M. B.: A comparative study of different
871 machine learning methods for landslide susceptibility assessment: A case study of Uttarakhand area
872 (India), *Environ Modell Softw*, 84, 240-250, <https://doi.org/10.1016/j.envsoft.2016.07.005>, 2016.
- 873 Preisig, G.: Forecasting the long-term activity of deep-seated landslides via groundwater flow and slope
874 stability modelling, *Landslides*, 17, 1693-1702, <https://doi.org/10.1007/s10346-020-01427-1>, 2020.
- 875 Ruitang, L., Zhaowei, C., Zexiong, W., Zhenghan, Z., Jiahao, L., Zhencheng, G., and Yuchong, C.:
876 Mountain Slope Monitoring Guidelines (TGS-SLOPEM106), 2017.
- 877 Simonyan, K. and Zisserman, A.: Very Deep Convolutional Networks for Large-Scale Image Recognition,
878 *ICLR2015*, <https://doi.org/10.48550/arXiv.1409.1556>, 2015.
- 879 Srivastava, S., Anand, N., Sharma, S., Dhar, S., and Sinha, L. K.: Monthly Rainfall Prediction Using
880 Various Machine Learning Algorithms for Early Warning of Landslide Occurrence, 2020 International
881 Conference for Emerging Technology (INCET), Belgaum, India, 5-7 June 2020, 1-7,
882 <https://doi.org/10.1109/INCET49848.2020.9154184>, 2020.



- 883 Stanton, J. M.: Galton, Pearson, and the Peas: A Brief History of Linear Regression for Statistics
884 Instructors, *Journal of Statistics Education*, 9, <https://doi.org/10.1080/10691898.2001.11910537>, 2001.
- 885 Szegeedy, C., Vanhoucke, V., Ioffe, S., Shlens, J., and Wojna, Z.: Rethinking the Inception Architecture
886 for Computer Vision, 2016 IEEE Conference on Computer Vision and Pattern Recognition (CVPR), 27-
887 30 June 2016, 2818-2826, <https://doi.org/10.1109/CVPR.2016.308>, 2016.
- 888 Thai Pham, B., Shirzadi, A., Shahabi, H., Omidvar, E., Singh, S. K., Sahana, M., Talebpour Asl, D., Bin
889 Ahmad, B., Kim Quoc, N., and Lee, S.: Landslide Susceptibility Assessment by Novel Hybrid Machine
890 Learning Algorithms, *Sustainability-Basel*, 11, <https://doi.org/10.3390/su11164386>, 2019.
- 891 van Natijne, A. L., Bogaard, T. A., Zieher, T., Pfeiffer, J., and Lindenbergh, R. C.: Machine-learning-
892 based nowcasting of the Vögelsberg deep-seated landslide: why predicting slow deformation is not so
893 easy, *Nat Hazard Earth Sys*, 23, 3723-3745, <https://doi.org/10.5194/nhess-23-3723-2023>, 2023.
- 894 Wang, Y., Dong, J., Zhang, L., Deng, S. H., Zhang, G. K., Liao, M. S., and Gong, J. Y.: Automatic
895 detection and update of landslide inventory before and after impoundments at the Lianghekou reservoir
896 using Sentinel-1 InSAR, *Int J Appl Earth Obs*, 118, <https://doi.org/10.1016/j.jag.2023.103224>, 2023.
- 897 Wu, J. H.: Seismic landslide simulations in discontinuous deformation analysis, *Comput Geotech*, 37,
898 594-601, <https://doi.org/10.1016/j.compgeo.2010.03.007>, 2010.
- 899 Xu, J., Jiang, Y., and Yang, C.: Landslide Displacement Prediction during the Sliding Process Using
900 XGBoost, SVR and RNNs, *Applied Sciences*, 12, <https://doi.org/10.3390/app12126056>, 2022.
- 901 Xu, J., Li, H., Du, K., Yan, C., Zhao, X., Li, W., and Xu, X.: Field investigation of force and displacement
902 within a strata slope using a real-time remote monitoring system, *Environmental Earth Sciences*, 77, 552,
903 <https://doi.org/10.1007/s12665-018-7729-3>, 2018.
- 904 Yang, B., Yin, K., Lacasse, S., and Liu, Z.: Time series analysis and long short-term memory neural
905 network to predict landslide displacement, *Landslides*, 16, <https://doi.org/10.1007/s10346-018-01127-x>,
906 2019.
- 907 Yang, S., Jin, A., Nie, W., Liu, C., and Li, Y.: Research on SSA-LSTM-Based Slope Monitoring and
908 Early Warning Model, *Sustainability-Basel*, 14, <https://doi.org/10.3390/su141610246>, 2022.
- 909 Zhang, L., Shi, B., Zhu, H., Yu, X. B., Han, H., and Fan, X.: PSO-SVM-based deep displacement
910 prediction of Majiagou landslide considering the deformation hysteresis effect, *Landslides*, 18, 179-193,
911 <https://doi.org/10.1007/s10346-020-01426-2>, 2021.
- 912 Zhang, W., Li, H., Tang, L., Gu, X., Wang, L., and Wang, L.: Displacement prediction of Jiuxianping
913 landslide using gated recurrent unit (GRU) networks, *Acta Geotechnica*, 17, 1367-1382,
914 <https://doi.org/10.1007/s11440-022-01495-8>, 2022.
- 915 Zhang, W. G., Zhang, R. H., Wu, C. Z., Goh, A. T. C., Lacasse, S., Liu, Z. Q., and Liu, H. L.: State-of-
916 the-art review of soft computing applications in underground excavations, *Geosci Front*, 11, 1095-1106,
917 <https://doi.org/10.1016/j.gsf.2019.12.003>, 2020.
- 918 Zhou, C., Yin, K., Cao, Y., Ahmed, B., and Fu, X.: A novel method for landslide displacement prediction
919 by integrating advanced computational intelligence algorithms, *Scientific Reports*, 8, 7287,
920 <https://doi.org/10.1038/s41598-018-25567-6>, 2018.
- 921 Zoph, B., Vasudevan, V., Shlens, J., and Le, Q. V.: Learning Transferable Architectures for Scalable
922 Image Recognition, 2018 IEEE/CVF Conference on Computer Vision and Pattern Recognition (CVPR),
923 <https://doi.org/10.1109/CVPR.2018.00907>, 2018.
- 924